J. Fluid Mech. (2008), *vol.* 611, *pp.* 175–204.
doi:10.1017/S0022112008001833 Printed in the United Kingdom

The near pressure field of co-axial subsonic jets

C. E. TINNEY† AND P. JORDAN

Laboratoire d'Etudes Aérodynamiques – UMR CNRS 6609,
CNRS, Université de Poitiers, ENSMA, France

(Received 2 November 2006 and in revised form 18 March 2008)

Results are presented from pressure measurements performed in the irrotational near field of unbounded co-axial jets. Measurements were made for a variety of velocity and temperature ratios, and configurations both with and without serrations on the secondary nozzle lip. The principal objective of the study is to better understand the near pressure field of the jet, what it can tell us regarding the underlying turbulence structure, and in particular how it can be related to the source mechanisms of the flow.

A preliminary analysis of the axial, temporal and azimuthal structure of the pressure field shows it to be highly organized, with axial spatial modes (obtained by proper orthogonal decomposition) which resemble Fourier modes. The effects of serrations on the pressure fluctuations comprise a global reduction in level, a change in the axial energy distribution, and a modification of the evolution of the characteristic time scales.

A further analysis in frequency–wavenumber space is then performed, and a filtering operation is used to separate the convective and propagative footprints of the pressure field. This operation reveals two distinct signatures in the propagating component of the field: a low-frequency component which radiates at small angles to the flow axis and is characterized by extensive axial coherence, and a less-coherent high-frequency component which primarily radiates in sideline directions. The serrations are found to reduce the energy of the axially coherent propagating component, but its structure remains fundamentally unchanged; the high-frequency component is found to be enhanced. A further effect of the serrations involves a relative increase of the mean-square pressure level of the acoustic component – integrated over the measurement domain – with respect to the hydrodynamic component. The effect of increasing the velocity and temperature of the primary jet involves a relative increase in the acoustic component of the near field, while the hydrodynamic component remains relatively unchanged: this shows that the additional acoustic energy is generated by the mixing region which is produced by the interaction of the inner and the outer shear layers, whereas the hydrodynamic component of the near field is primarily driven by the outer shear layer.

1. Introduction

The near irrotational pressure field in the periphery of an unbounded jet has been the subject of a considerable number of experimental and theoretical investigations over the past 60 years (Mayes, Lanford & Hubbard 1959; Howes 1960; Mollo-Christensen 1963; Keast & Maidanik 1966; Ollerhead 1967; Arndt *et al.* 1997; Ricaud 2003; Reba *et al.* 2005; Coiffet *et al.* 2006; Barre *et al.* 2006; Suzuki & Colonius 2006), from which researchers have endeavoured to better understand

† Current address: Department of Aerospace Engineering and Engineering Mechanics, University of Texas at Austin, Austin, TX 78712, USA.

the nature of the large-scale flow dynamic and its sound production mechanisms. This measurement approach presents a number of advantages. Pressure is a scalar quantity, acting as a natural wavenumber filter (George, Beuther & Arndt 1984), and near-field measurements are relatively non-intrusive. It is for these reasons that Keast & Maidanik (1966) suggest that such measurements present 'a unique means for studying turbulence'.

Certain difficulties exist however concerning physical interpretation of the pressure field in this region of the flow, and in particular when relating it to the underlying turbulence, and/or sound production mechanisms. On one hand, the near pressure field is dominated by dynamics which are best described by a linear hyperbolic differential equation, whereas it is essentially driven by a nonlinear hydrodynamic pressure field which is well approximated by elliptic equations. Some qualification is therefore required where interpretation of near field measurements in terms of the underlying turbulence is concerned. The following observations are helpful in this regard. The pressure intensity in the non-linear hydrodynamic region (the rotational part of the flow) is characterized by $kr^{-7/3}$ (George *et al.* 1984), in the linear hydrodynamic region (irrotational near field) by $kr^{-6.67}$ (Arndt *et al.* 1997) and in the linear acoustic region by kr^{-2} (Arndt *et al.* 1997) where kr is a non-dimensional wavenumber (k and r are acoustic wavenumber and distance respectively). In the linear hydrodynamic region of the flow, for a given wavenumber, there is a very rapid spatial decay, and so pressure signatures registered in this region can be considered to constitute relatively local information concerning the large turbulence structures which are predominant in driving this part of the pressure field (Howes 1960; Picard & Delville 2000; Ricaud 2003; Coiffet *et al.* 2006; Tinney *et al.* 2007). Howes (1960) has pointed out that because of this very rapid attenuation of the fluctuating pressure level as a function of source–observer distance, while the entire turbulent region contributes to any given near field observation point, the pressure fluctuations at that near-field point are very strongly determined by the turbulence in the flow immediately adjacent.

There is however a further difficulty, related to the hyperbolic dynamics of the near field, and which hinders clear interpretation of near field measurements. In addition to comprising a hydrodynamic signature of the turbulence in the rotational region of the jet, the near field also contains the beginnings of a sound field which is destined to reach the far field. Howes (1960) has discussed how a microphone in the near field will be subject to fluctuations associated with incompressible 'pseudosound', which does not radiate, and compressible propagating sound waves; while Mollo-Christensen (1963) similarly points out that while the phenomena measured are related to hydrodynamic instabilities, part of what is observed corresponds to sound waves propagating downstream in the jet. It is clear that the underlying physical processes merit a more detailed study. Indeed, interpretations of near-field measurements in terms of the underlying turbulence structure will be susceptible to error if this point is overlooked: acoustic contributions exist and it is difficult to ascertain to what degree. We address this issue here in some detail.

As we are dealing with co-axial jets, in addition to those discussed above we have the further complications which arise on account of the existence of two shear layers; these are characterized by different velocity and temperature gradients, turbulence scales, and characteristic convection velocities. And, as each of the shear layers can be expected to generate sound independently in the initial regions of the jet, there is also the problem of understanding to what extent the structure of the near field is governed by the generation and refraction of sound by the two shear flow regions. Some of these issues are discussed in more detail in § 5 where we study the frequency–wavenumber content of the near field.

We study the near pressure fields in the irrotational periphery of a number of subsonic co-axial jets by means of linear and azimuthal microphone arrays, with a view to better understanding how changes in the jet exit conditions (velocity ratio, temperature ratio and in particular nozzle serrations) modify the large-scale behaviour of the flow and its radiated sound. Measurements in flows of this kind, which are closer to the flows characteristic of full-scale jet engines than most laboratory-scale flows, are lacking in the scientific literature, and so in addition to the provision of a number of interesting physical insights, this work constitutes a benchmark for comparison with future simulations and experiments.

In an initial phase the temporal, axial and azimuthal characteristics of the pressure fields are assessed by conventional statistical means in order to establish a basic understanding of the flows' irrotational near fields. The second-order statistical moments are studied, and correlation and Fourier analyses used in (x, θ, t) to understand the spectral make-up of the pressure field. This analysis confirms previous work, showing the near pressure field to be highly organized. The main effect of the nozzle serrations involves a global reduction in the fluctuation energy of the field, and a dramatic reduction in the axial amplification of near field fluctuations; however, in terms of axial and azimuthal coherence the serrations produce very little change, showing that structural changes in the near field are very slight. An extensive study is also performed using proper orthogonal decomposition (POD), and we assess the proximity of the POD basis-function set to a Fourier basis-function set.

A further analysis is then focused on the question of the relative importance of contributions from hydrodynamic pressures, and from propagating acoustic pressures, both of which, as discussed above, are present in the near field. With the exception of the work of Arndt *et al.* (1997) and Coiffet *et al.* (2006), this element has rarely featured in near field pressure analyses. By considering the phase-velocity signature characteristic of a propagating wave field, a filtering operation is performed which permits the isolation of fluctuations related to propagating acoustic modes. This allows the hydrodynamic and acoustic components to be studied separately. The serrations are found to dramatically reduce both; however, the relative contribution of the acoustic component is found to increase. Increasing the velocity and temperature of the primary jet causes very little change in the hydrodynamic component of the pressure field, while the acoustic component is enhanced. This shows that the hydrodynamic near field signature is primarily driven by the outer shear layer, and that the increased levels which are observed, as the primary jet velocity and temperature increase, are due almost entirely to a more energetic acoustic field associated with the additional mixing region which is produced by the interaction of the inner and the outer shear layers.

The paper is organized as follows. In § 2, detailed descriptions of the experiment and the flow configurations studied are provided. Section 3 is devoted to a presentation and discussion of the trends identified by conventional statistical, correlation and spectral analyses, and in § 4 the structure of the pressure field is assessed using POD. In § 5 a filtering operation which allows the extraction of supersonic components of the pressure field is described, and the filtered fields are presented and discussed. This is followed by a summary of the results in § 6.

2. Experimental setup

2.1. *Instrumentation and flow conditions*

Measurements were performed in the near field regions of jets issuing from two short-cowl axisymmetric co-axial nozzles. The two geometries investigated were a

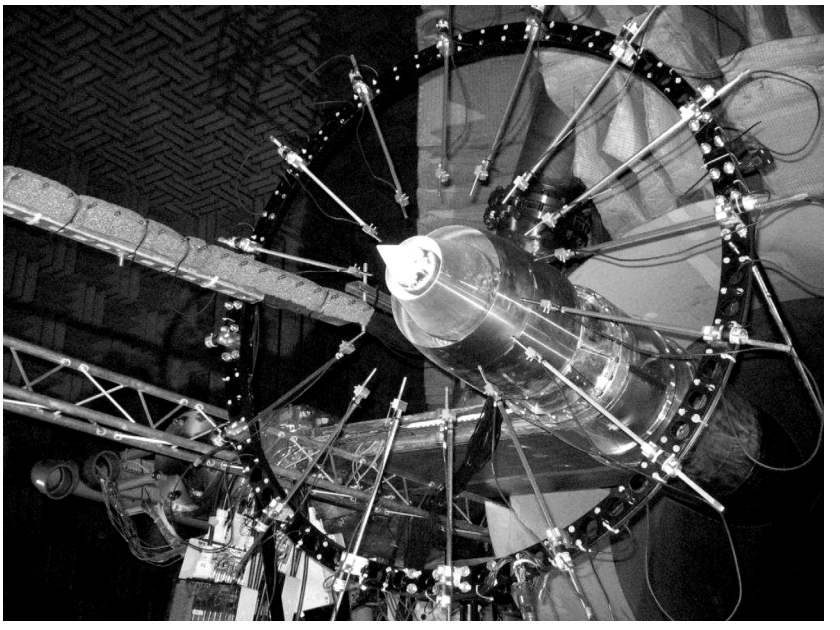

FIGURE 1. Experimental arrangement of the short-cowl co-axial nozzle (SCN) with the azimuthal and line arrays of microphones at the Noise Test Facility (NTF), QinetiQ.

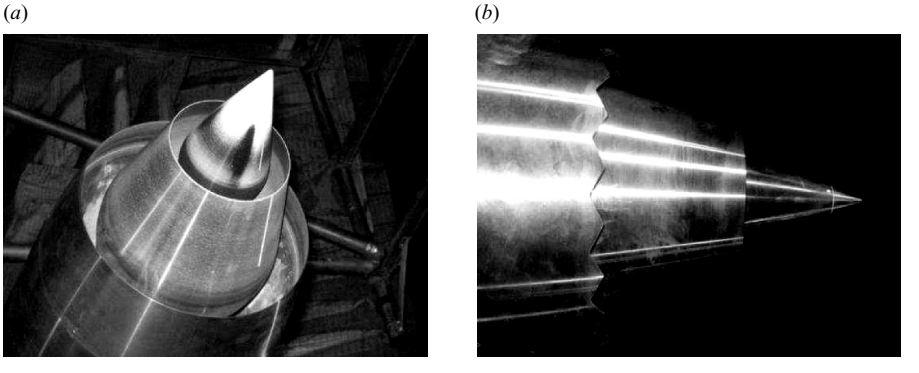

FIGURE 2. (*a*) Short-cowl nozzle (SCN). (*b*) Short-cowl nozzle with 20 serrations (SN).

short-cowl configuration without serrations (Short-Cowl Nozzle hereafter SCN) and one with serrations (Serrated Nozzle hereafter SN) located on the secondary nozzle nacelle (20 equi-spaced serrations). As serrations are known to suppress the far field sound (Tester & Fisher 2006; Brown & Bridges 2006), the experiment provides an opportunity to understand differences between baseline and noise-controlled flows.

The experiments were conducted at the QinetiQ Noise Test Facility (NTF) at Farnborough, UK. The microphone arrays are shown in figure 1, the nozzles in figure 2(*a*, *b*). For each of the co-axial nozzles, short-cowl (SCN in figure 2*a*) and short-cowl with serrations (SN in figure 2*b*), the total temperature (T_o) and bypass ratios (U_s/U_p) were varied according to the three conditions shown in table 1, where the subscripts p and s denote primary and secondary nozzles/jets, respectively. The gas-dynamic sound speed, included in parentheses in table 1, was computed based on the

Condition	$U_s(a_s)$ [m s^{-1}]	$U_p(a_p)$ [m s^{-1}]	U_s/U_p	T_{so} [K]	T_{po} [K]	T_{so}/T_{po}
1	307 (367)	340 (577)	0.90	335	828	0.40
2	307 (367)	405 (584)	0.76	335	850	0.39
3	307 (367)	481 (595)	0.64	335	880	0.38

TABLE 1. Table of jet exit conditions for both nozzle geometries.

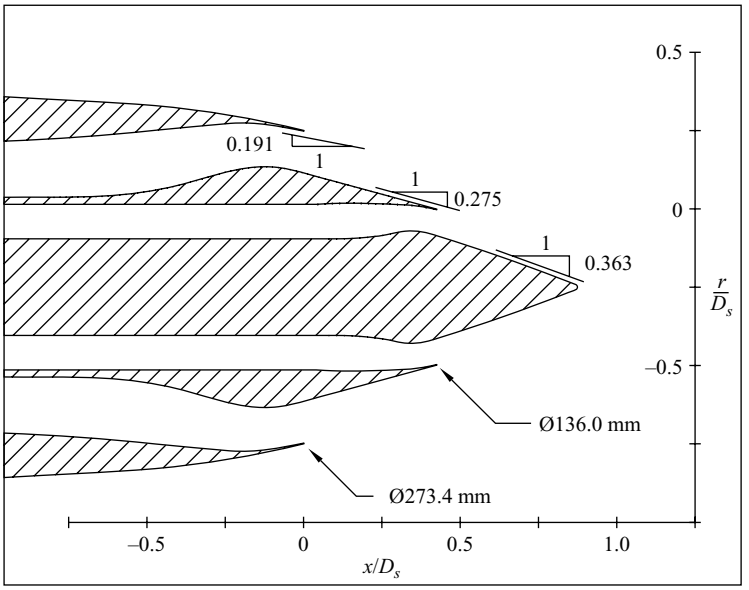

FIGURE 3. Short-cowl nozzle geometry.

corresponding flow temperature (primary or secondary) using $a = \sqrt{\gamma RT_o}$ and values for the gas constant (R) and the ratio of specific heats (γ) of 287 J kg^{-1} K^{-1} and 1.4, respectively. The sound speed for the ambient field (a_a) using $T = 288°$K is 341 m s^{-1}. A more detailed drawing, showing all relevant dimensions of the SCN geometry, is shown in figure 3; apart from the serrations, the internal SN profile is the same.

The design of the experiment followed that of the single-stream jet measurements of Ricaud (2003). A line array of 48 microphones was mounted so as to follow the expanding jet (expansion estimated to be around 8.5° based on preliminary PIV measurements) with the first microphone tip located at a radial distance of 6.5 cm from the secondary nozzle lip at the exit plane of the secondary nozzle at $x/D_s = 0$ and an inter-microphone spacing of 50 mm. A circular array comprising fifteen microphones (the sixteenth being the one on the line array) was used to measure the azimuthal pressure field at nine axial stations. These nine stations are indicated in figure 6 by '$\star$' and were the same for both nozzles and all three exit conditions. For each microphone on the azimuthal array, a dedicated servo-motor moved it radially to match the radial position of the reference microphone on the line array for each new axial station to which the azimuthal array was traversed.

The 1/4 in. microphones and matching preamplifiers were MICROTECH GEFELL type MK301 and MK302, respectively, and were sampled at $f_s = 24096$ Hz for 5 seconds using 24 bit accurate A/D converters over a ± 3 v bipolar range. The MK301

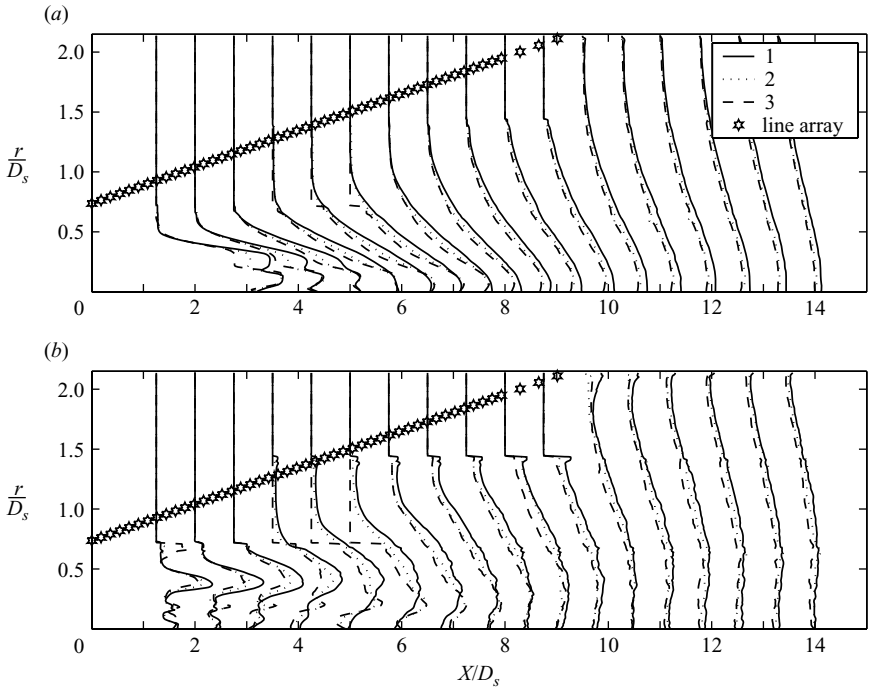

FIGURE 4. Axial (a) mean (U/U_{cl}) and (b) turbulence (u'/U_{cl}) velocity ratios of the SCN flow for all exit conditions (1,2,3) relative to the microphone line array.

free-field condenser microphone is side vented (it measures fluctuating quantities only) with a frequency response range between 5 Hz and 100 kHz ($\pm$2dB) for sound pressure levels up to 168 dB.† Based on the nozzle exit conditions illustrated in table 1, the largest time scales of the flow estimated from U_s/D_s, where D_s is 273.4 mm, indicate that there were a minimum of 2700 statistically independent samples.

Mean and turbulence velocity profiles of the SCN flow are shown in figure 4(a, b) to provide a qualitative picture of the coaxial jet flow, and its position with respect to the line array of microphones. These profiles were acquired from particle image velocimetry (PIV) measurements performed (by the University of Warwick, see Skeen 2007) along the (r, x)-plane of the jet; the line array is shown to be located sufficiently far from the shear layer so as not to be subjected to any flow forcing effects. These velocity profiles are qualitatively similar to the co-axial jet flow measurements of Ko & Kwan (1976): the two turbulent mixing layers from the primary and secondary jet streams eventually merge to form a single mixing region which further develops into a fully developed turbulent far field. The geometries of the short-cowl and serrated nozzles closely resemble current commercial propulsion systems (figure 2a, b), and an effect of the centrebody on the mean flow profiles can be seen in figure 4(a) at $r/D_s = 0$ in the form of a mean velocity deficit that persists until $x/D_s = 3.5$.

Unphysical data points caused by the edge of the PIV camera measurement window are seen in the turbulence profiles in figure 4(b) at $r/D_s = 1.5$. These profiles are presented only to show the global features of the co-axial jet flow relative to the line array.

† Specific information for these instruments can be found at http://www.microtechgefell.de.

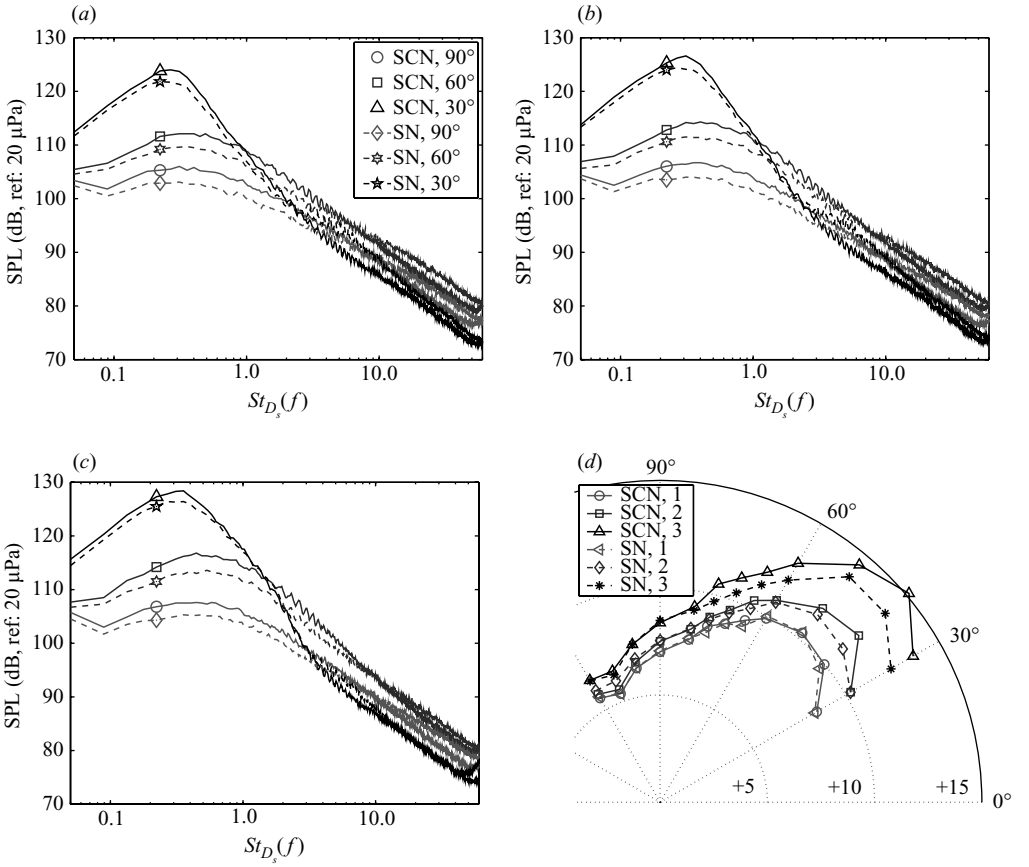

FIGURE 5. Far-field acoustic surveys: (*a*) condition 1, (*b*) condition 2, (*c*) condition 3, (*d*) diroctivity.

3. Preliminary results and discussion

3.1. *Far-field acoustic surveys*

The far field acoustic measurements are presented here for reference; these were acquired using an arc array of 1/2 in. microphones between 120° and 30° from the jet axis. The pressure spectral densities and overall sound pressure level (OASPL) directivity are shown in figure 5 for three far field microphones located at 90°, 60°, and 30°, centred on the jet exit, and at radial distances of $48D_s$, $45D_s$, and $43D_s$, respectively. The spectral densities were calculated using a 50 Hz narrow-band average. The effect of the serrations can be seen to comprise a low-frequency reduction and a high-frequency increase; the cross-over frequency is a function of emission angle. Similar trends have been observed by Brown & Bridges (2006), Tester & Fisher (2006) and Alkislar, Krothapalli & Butler (2007).

The overall far field level and spectral peak can also be seen to increase as the primary jet velocity and temperature are increased. At exit condition 1 a peak level of 124 dB is observed at $St_{D_s} = fD_s/U_s = 0.29$, while for condition 3 a level of 128 dB is observed at $St_{D_s} = 0.32$.

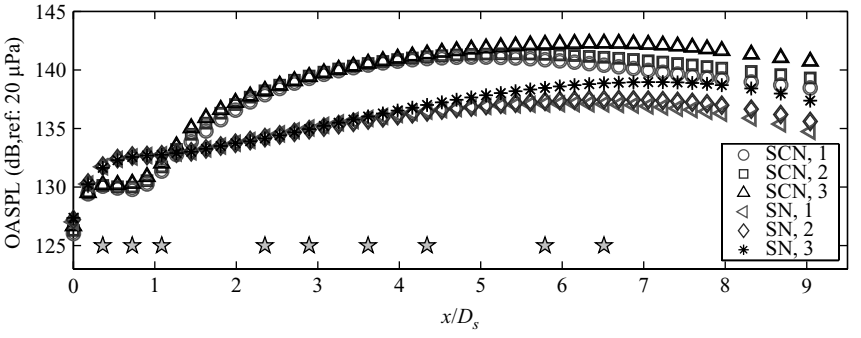

FIGURE 6. Overall sound pressure level (OASPL) profiles for all conditions of the SCN and SN flows.

3.2. *Near-field OASPL profiles*

Axial profiles of the OASPL, shown in figure 6, give a preliminary indication of the effect of both nozzle geometry and exit condition. The effect of the serrations is clear: fluctuating pressure levels in the near-nozzle region ($0 < x/D_s < 1$) are increased, while for $x/D_s > 1$ the axial evolution of the pressure field is characterized both by considerably reduced levels (5 dB) and a change in shape. The rapid amplification characteristic of the OASPL for the SCN flow in the region $1 < x/D_s < 6$ is calmed by the serrations. Further downstream the SN flow signature recovers an evolution similar to that of the SCN flow. For a given nozzle, differences due to changes in the jet exit conditions are most pronounced farther downstream: near-field levels are seen to increase as the bypass and temperature ratios decrease.

3.3. *Near-field spectra*

Auto-spectral densities (expressed as sound pressure level, SPL) computed from the line array data are shown in figure 7(a–d); a 5% bandwidth moving filter has been used. The bin size comprised $M = 4096$ samples, resulting in a spectral resolution δf of 5.88 Hz. As seen in the OASPL profiles, the serrations produce a reduction in the pressure fluctuations everywhere except in the near-nozzle region, where a broadband increase is manifested for all frequencies except those concentrated around the spectral peak ($0.5 < St_{D_s} < 2$). Changes in the exit condition can be seen to produce only very negligible changes in the peak regions of the spectra, the principal changes occuring at higher Strouhal numbers. On closer inspection of figure 7 it can be seen that the axial evolution of the spectral peak is changed by the serrations. This can be more clearly seen in figure 8(a, b): the serrations are seen to modify the evolution of the spectral peak; the shift in the characteristic time scale of the SN pressure field is less abrupt than that of the SCN pressure field, which undergoes a larger and more rapid change from high to low frequency. This was observed for all three exit conditions.

3.4. *Space–frequency coherence – hydrodynamic and acoustic signatures*

Coherence spectra from microphones on the line array are shown in figure 9(a, b) for reference microphones at four axial stations. These are shown for the first nozzle exit condition only, as changes in the exit conditions were found to produce negligible changes. These plots furnish information concerning the nature of the pressure fluctuations at different frequencies.

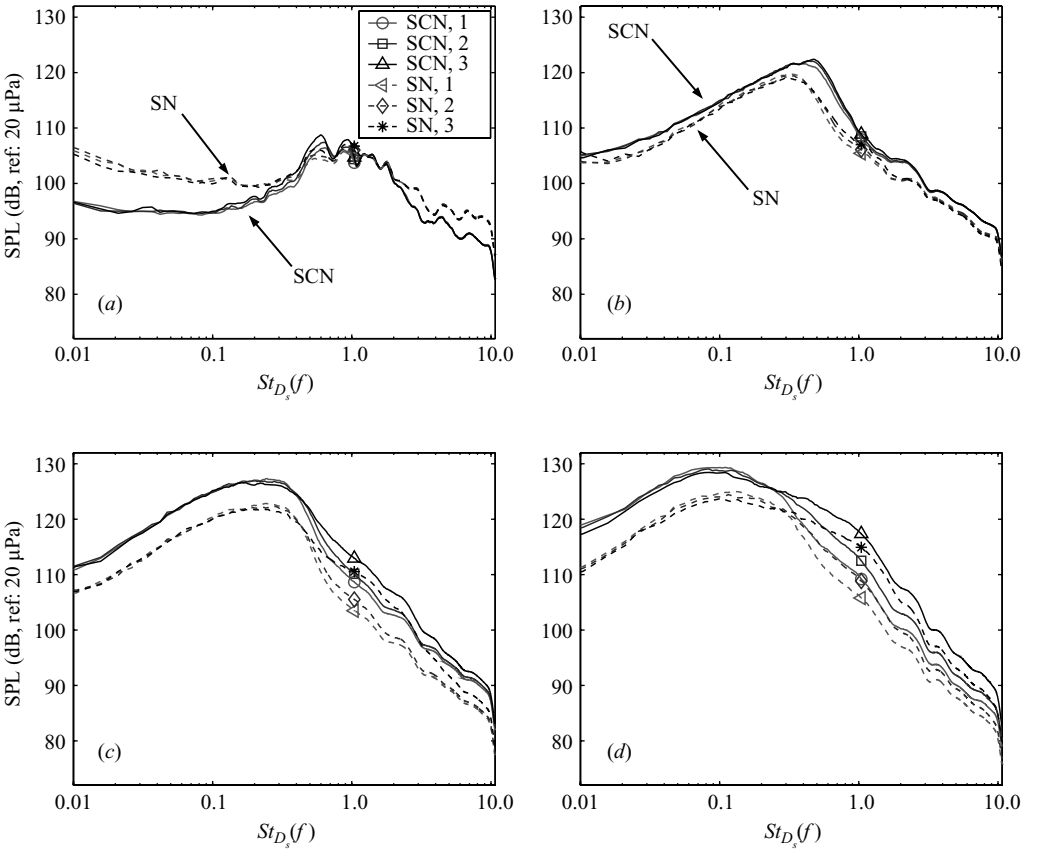

FIGURE 7. Pressure spectra of both nozzles and all three exit conditions at $x = (a)\ 0D_s$, $(b)\ 2D_s$, $(c)\ 4D_s$ and $(d)\ 6D_s$.

It has previously been argued by Arndt *et al.* (1997) and Coiffet *et al.* (2006) that a reasonable *ad-hoc* separation of the near field spectra into regions dominated by hydrodynamic and acoustic fluctuations can be effected by dividing the spectra into a low-frequency hydrodynamic regime and a high-frequency acoustic regime. Arndt *et al.* (1997), Harper-Bourne (2004) and Coiffet *et al.* (2006) identify Helmholtz numbers lying in the range $1 < kr_s < 2$ for a simple round jet (where k denotes the wavenumber and r_s is the radial distance measured from the centre of the jet shear layer) as the demarcation point. The spectra can be seen to comprise two such regimes, $0 < St_{D_s} < 0.75$ and $St_{D_s} > 0.75$, most marked in the range $0 < x/D_s < 5$. In the low-Strouhal-number regime $0 < St_{D_s} < 0.75$ the pressure field is characterized by extensive axial coherence, corresponding to a convective signature related to the coherent structures of the flow, whereas at higher Strouhal numbers the axial coherence is considerably less extensive – the signature of a more chaotic sound field radiating in many different directions from an extended distribution of sources. The abruptness of the switch from hydrodynamic to acoustic dominance is striking, and similar to the results of Arndt *et al.* (1997) and Coiffet *et al.* (2006) for measurements performed in the near field of single-stream jets.

For all of the data presented so far interpretations have been hampered by the uncertainty in whether the trends identified pertain to hydrodynamic or acoustic

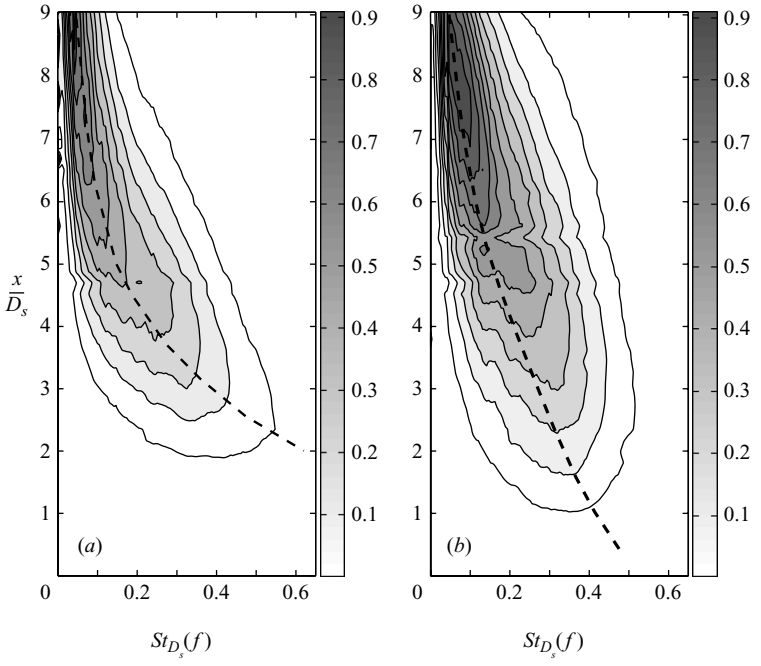

FIGURE 8. Pressure spectra contours for condition 1 of the (*a*) SCN and (*b*) SN jets. Each contour has been normalized by its maximum value, while the decrement level has been set to 0.1.

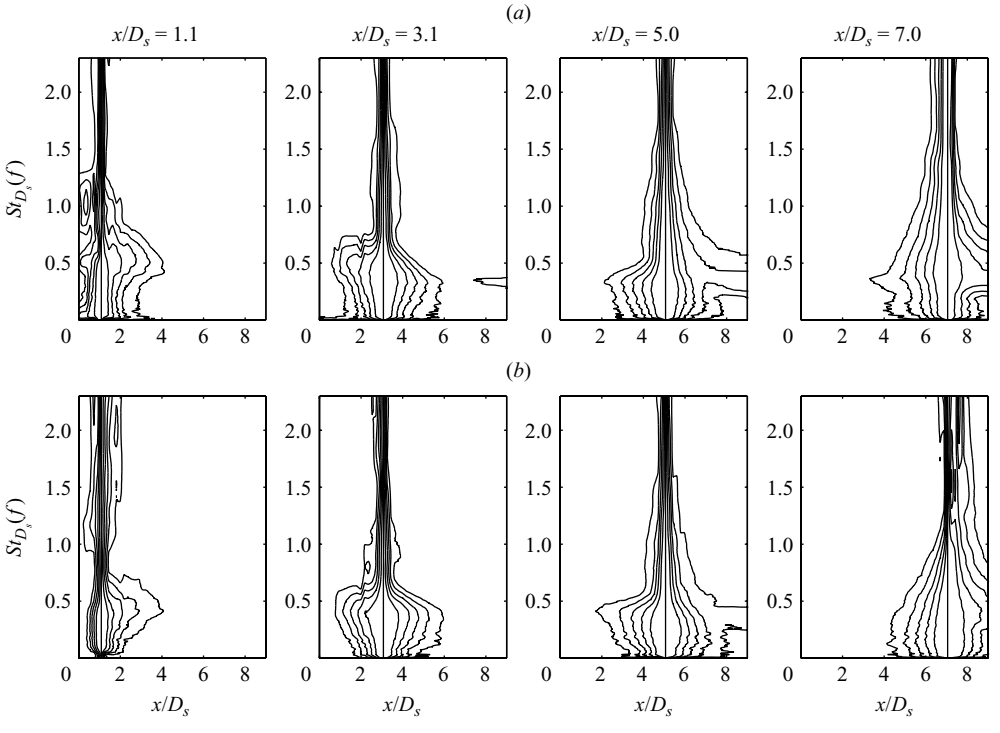

FIGURE 9. The coherence spectra at various axial positions of the reference microphone for the (*a*) SCN, and (*b*) SN flows under condition 1.

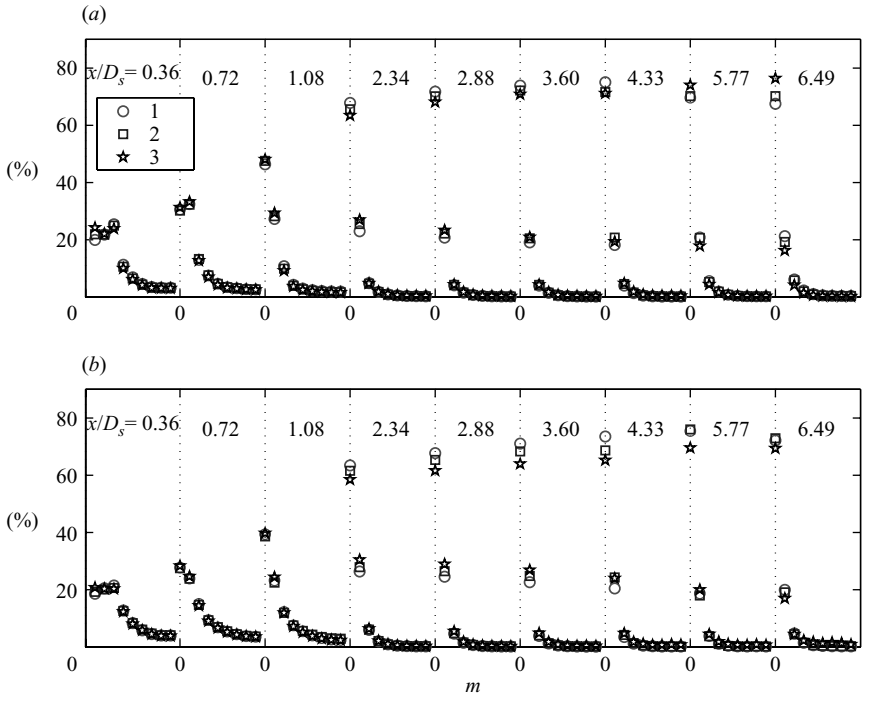

FIGURE 10. Fourier-azimuthal modes of the (*a*) SCN and (*b*) SN near pressure fields at various axial locations in the flow. The zeroth mode is identified as the start of each axial station.

fluctuations. Using the same *ad-hoc* separation as Arndt *et al.* (1997) and Coiffet *et al.* (2006), it appears that the major changes produced by changes in the bypass and temperature ratios, as shown in figure 7, correspond to changes in the radiated sound field, rather than to changes in the hydrodynamic signature. The axial evolution of the near field spectra suggests that the acoustic and hydrodynamic regimes follow the same behaviour up to about $x/D_s \sim 4$; farther downstream however, the acoustic energy clearly increases with decreasing bypass and temperature ratios. This also implies that changes observed in the axial OASPL profiles for changes in the jet exit conditions (figure 6) are related to the acoustic component of the near pressure field. This trend indicates that while the large-scale structure of the flow (as sensed by the near-field array) has not undergone any dramatic modification, the sound energy radiated from the flow has changed considerably. As the change in the exit conditions involves an increase in the primary jet's velocity and temperature, the relatively invariant low-frequency part of the near-field spectrum suggests that the near field is principally driven by the secondary flow instabilities.

3.5. *The azimuthal structure of the near field*

A Fourier-azimuthal decomposition using data acquired by the azimuthally arranged microphones is shown in figure 10(*a*, *b*). These results are consistent with previous studies of the near pressure field of axisymmetric jets by Ko & Davies (1971), Arndt *et al.* (1997), Jordan *et al.* (2005) and Tinney *et al.* (2007), where the most coherent low-order turbulence structures have been found to be most efficient in driving the near field pressure. Again we see that there are only small differences, in terms of azimuthal orgonization, of the near pressure fields generated by the nozzles with

and without serrations. For a more detailed analysis of these data in terms of the azimuthal orgonization of the pressure field refer to Guerin & Michel (2006)

3.6. *Summary of initial observations*

Summarizing the results presented so far, the significant changes produced in the near pressure field by the serrations were found to comprise:

(i) a considerable reduction (overall) in the fluctuating near field pressure levels;

(ii) a change in the axial distribution of the fluctuation energy, as reflected by the OASPL, over the first 6 diameters (D_s);

(iii) a less dramatic shift in the axial evolution of the peak Strouhal number.

On the other hand the serrations were not found to produce such marked changes in either the axial coherence of the flow structure, or its azimuthal modal composition. An *ad-hoc* method, taken from Arndt *et al.* (1997) and Coiffet *et al.* (2006), for understanding the composition of the pressure field in terms of hydrodynamic and acoustic contributions was used to show that the principal effect of changes in the exit condition comprise a change in the radiated sound pressure, this change being mostly seen in the region beyond $x/D_s \sim 4$, negligible changes being observed in the hydrodynamic flow signature. The insensitivity of the hydrodynamic part of the near field spectra to changes in the bypass ratio was interpreted as an indication that the near field is primarily driven by the flow structures from the secondary-jet outer shear layer.

4. Proper orthogonal decomposition of the pressure field

We here use POD to further study the axial structure of the near pressure field. The application of this technique has been well documented (Glauser & George 1987; Aubry *et al.* 1988; Berkooz, Holmes & Lumley 1993; Delville *et al.* 1999). As the foregoing analysis has included both the time-averaged and spectral characteristics of the pressure field, the POD is applied using two different forms for the kernel: one comprising time-averaged correlations,

$$R_t(x, x') = \langle p(x, t)p(x', t)\rangle, \tag{4.1}$$

and a second using an ensemble average of cross-spectral densities

$$R_f(x, x'; f) = \frac{1}{2\pi}\int_{-\infty}^{\infty} \langle p(x, t)p(x', t+\tau)\rangle \mathrm{e}^{-\mathrm{i}2\pi f\tau}\,\mathrm{d}\tau. \tag{4.2}$$

Each of the problems reduces to a Fredholm integral equation of the first kind:

$$\int R_t(x, x')\phi^{(n)}(x')\,\mathrm{d}x' = \lambda^{(n)}\phi^{(n)}(x), \tag{4.3}$$

and

$$\int R_f(x, x'; f)\Phi^{(n)}(x'; f)\,\mathrm{d}x' = \Lambda^{(n)}(f)\Phi^{(n)}(x; f), \tag{4.4}$$

where $\lambda^{(n)}$, $\Lambda^{(n)}$ and $\phi^{(n)}$, $\Phi^{(n)}$ are the proper values (representative of the energy content) and proper functions (representative of the characteristic signal), respectively. We have chosen to use upper and lower case lettering to distinguish the POD which uses a time-suppressed kernel $R_t(x, x')$ from that which employs a frequency-dependent kernel $R_f(x, x'; f)$. While the integral problems (4.3) and (4.4) each produce a denumerable set of discrete solutions, they are limited in practice to the number of

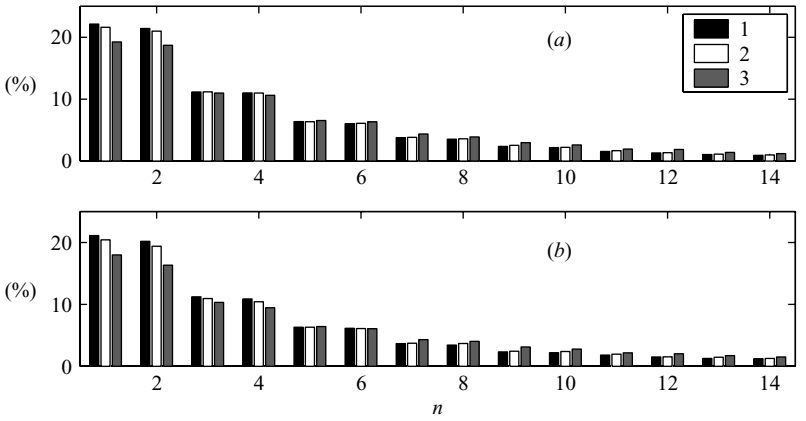

FIGURE 11. Convergence of the POD eigenvalues $\lambda^{(n)}$ from the decomposition of the (*a*) SCN and (*b*) SN flows for all three exit conditions.

spatial positions measured ($N = 48$). In the case of (4.4), the integral problem is solved independently for each frequency, and this permits identification of the characteristic frequencies associated with each discrete solution.

The proper functions and proper values (hereafter referred to as eigenfunctions and eigenvalues) can be used to expand the kernel as follows:

$$\mathscr{R}_t^{(m)}(x, x') = \sum_{n=1}^{m} \lambda^{(n)} \phi^{(n)}(x) \phi^{(n)}(x'), \tag{4.5}$$

$$\mathscr{R}_f^{(m)}(x, x'; f) = \sum_{n=1}^{m} \Lambda^{(n)}(f) \Phi^{(n)}(x; f) \Phi^{(n)*}(x'; f), \tag{4.6}$$

where $\mathscr{R}_t^{(m)}(x, x') = R_t(x, x')$ and $\mathscr{R}_f^{(m)}(x, x'; f) = R_f(x, x'; f)$ for $m = N$. By truncation of the convergent series (i.e. $m < N$), a low-order approximation of the kernel is obtained which can provide insight into the spatial structure of the flow features which are best correlated with the energy-integrable field (Aubry *et al.* 1988).

The convergence of the eigenvalues $\lambda^{(n)}$ from (4.3) are shown in figure 11 for both nozzles and all three jet exit conditions. The eigenvalues are normalized by their total cumulative energies, i.e. $\sum_n \lambda^{(n)}$, and are shown only for the first 14 POD modes, as subsequent modes contribute very little. It is well known that if the eigenvalues converge rapidly, the fluctuating field can be considered to comprise a superposition of organized coherent events, slow convergence being indicative of less coherent events. The eigenspectra shown in figure 11 show a decrease in amplitude of the first few POD modes with decreasing bypass ratio, whereas for the higher modes an increase in energy is observed. As the different exit conditions have only noticeably affected the higher frequencies in the pressure field (figure 7*a–d*), the two trends observed (relative decay in energy of the first few POD modes, relative increase in energy of the higher POD modes) can be associated with the observed increase in the higher frequency activity (associated with the 'acoustic' field from the discussion in § 3.3).

A low-order reconstruction of the kernel is performed using (4.5) and the two most energetic eigenfunctions from (4.3). Figure 12(*a*) shows: $\mathscr{R}^{(1,2)}(x, x)$ (simply the diagonal of the kernel matrix), their sum $\mathscr{R}^{(1+2)}(x, x)$, and the original mean-square pressure profile from the SCN flow at condition 1. An amplification–saturation–decay

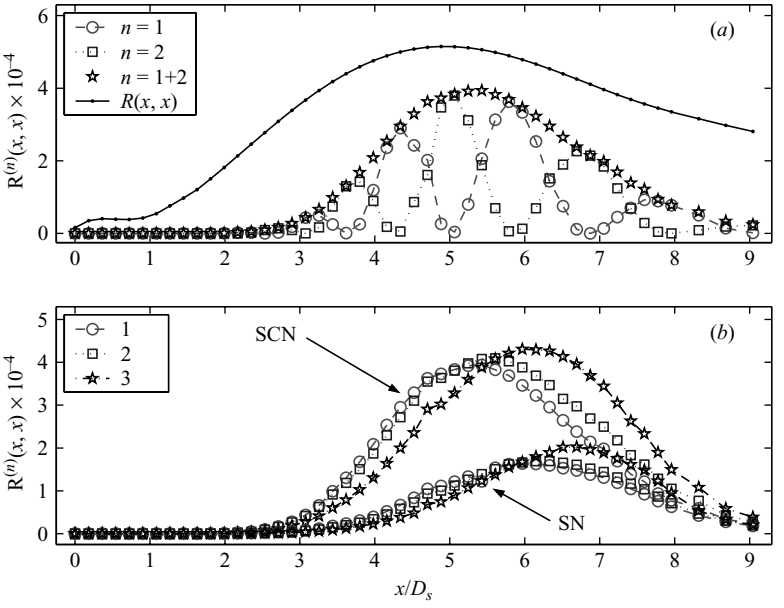

FIGURE 12. (*a*) Low-dimensional reconstruction of the diagonal part of the kernel from the SCN flow and condition 1. (*b*) Cumulative reconstructions of the diagonal part of the kernels using POD modes 1 and 2 for both co-axial nozzles and all three exit conditions.

envelope of the axial structure is manifest, and the change to this envelope produced by changes in the exit condition is shown in figure 12(*b*) for both nozzles and all three exit conditions. It can be seen how roughly the same evolution occurs with exit condition for both the SN and SCN flows. However, an effect of the serrations is to suppress amplification and move the peak further downstream.

The first two eigenvalues $\Lambda^{(1,2)}(f)$ of the frequency-dependent solution of the POD from (4.4), are shown in figure 13(*a*, *b*), for both nozzles and all three exit conditions. This illustrates the spectral characteristics of the two most energetic eigenvalues of the axial pressure field. Since the total resolved kinetic energy (E) is equal to the sum of the eigenvalues (Citriniti & George 2000),

$$E = \int \langle p(x;f)p^*(x;f)\rangle \,\mathrm{d}x = \sum_{n=1} \Lambda^{(n)}(f), \tag{4.7}$$

the energy in the first few eigenvalues can exceed that of any of the auto- and cross-spectral densities of the kernel. This is apparent in figure 13(*a*, *b*) where the energy of the eigenvalues is greater than any of the individual spectral densities shown in figure 7(*a–d*).

As seen in the pressure spectra (figure 7*a–d*), the different jet exit conditions have little effect on the most energetic regions of the pressure eigenspectra, which is dominated by the low-frequency hydrodynamic fluctuations: the footprint of the large scale turbulence structure. The higher frequencies, on the other hand, have been affected. For a given nozzle geometry, the higher-frequency energy increases with increasing temperature and velocity. This is an indication that the first two POD modes also contain some contribution from these acoustic fluctuations, implying that some component of the latter may comprise a relatively coherent signature.

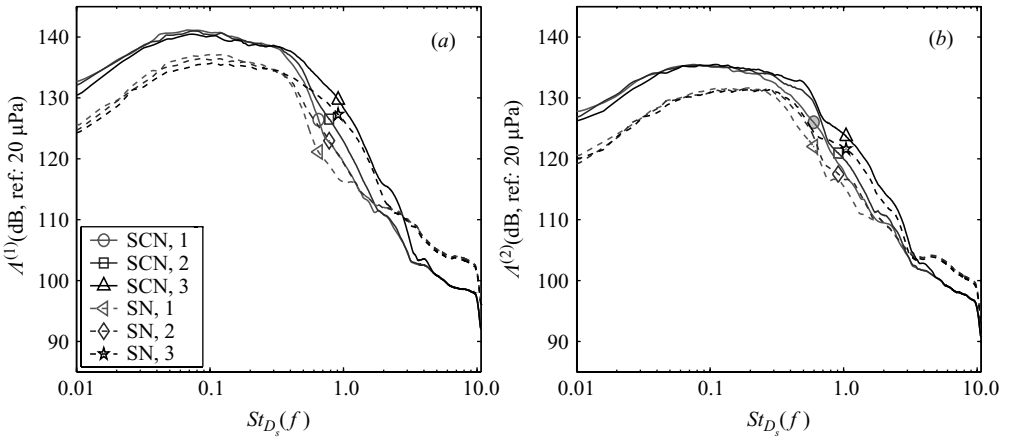

FIGURE 13. Spectral energy distribution of $\Lambda^{(n)}(f)$ for the (*a*) $n=1$ and (*b*) $n=2$ POD modes.

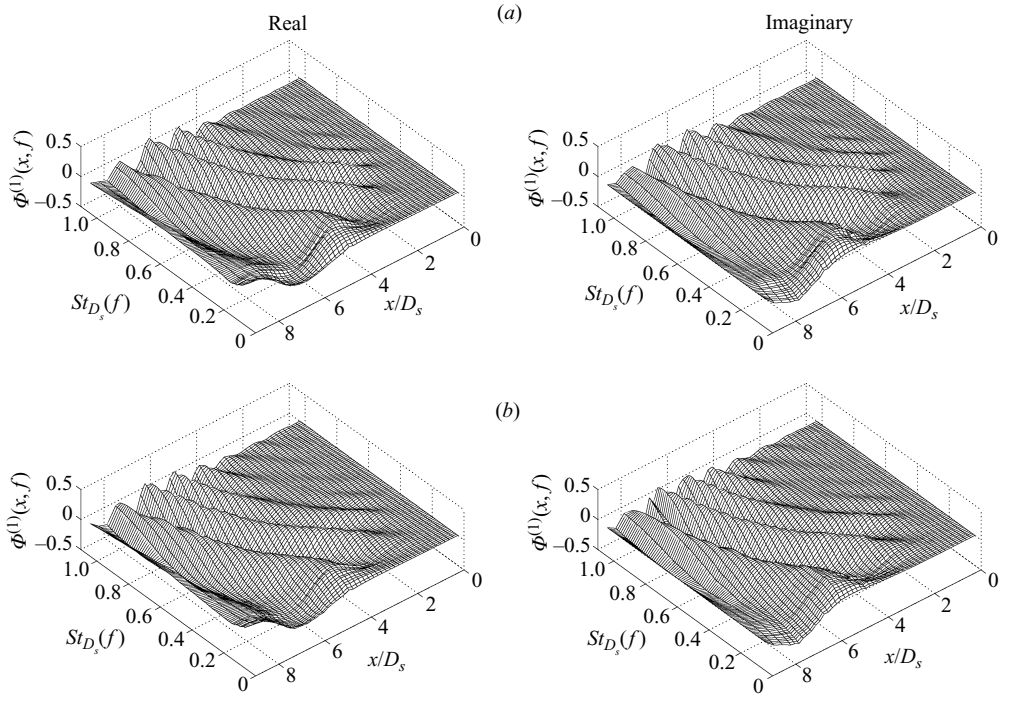

FIGURE 14. Spectral energy distribution of the first POD eigenfunction $\Phi^{(1)}(x, f)$ from the (*a*) SCN and (*b*) SN flows at condition 3. The left and right columns pertain to the real and imaginary components of the complex eigenfunctions, respectively.

The real and imaginary components of the first eigenfunction $\Phi^{(1)}(x; f)$ obtained from the spectral decomposition are shown in figure 14(*a–d*) for the SCN and SN flows at condition 3, as a function of Strouhal number and spatial position in the flow (x). These are similar to results from single-stream jet studies of Arndt *et al.* (1997) and Jordan *et al.* (2005). Once again, this axial structure is seen to comprise waveforms which amplify, saturate and decay with their downstream evolution. The importance of this process with regard to the production of sound by a jet has been discussed

by Ffowcs Williams & Kempton (1978) and Crighton & Huerre (1990). Lower-frequency activity is characterized by low axial wavenumbers (large wavelengths) and saturation positions located toward the downstream limit of the measurement domain, while higher-frequency activity is characterized by higher wavenumbers (smaller wavelengths) and saturation locations closer to the jet exit.

4.1. *Scale homogeneity*

A striking feature of the eigenspectra in figure 11 is that the energy of the eigenvalues is organized in pairs for both nozzles and all three exit conditions, that is $\lambda^{(1)} \simeq \lambda^{(2)}, \lambda^{(3)} \simeq \lambda^{(4)}, \ldots \lambda^{(N-1)} \simeq \lambda^{(N)}$. As discussed by Lumley (1967, 1981), POD reduces to a harmonic orthogonal decomposition when the direction of the treated field is homogeneous, periodic or stationary. Of course harmonic modes are continuous functions, whereas POD modes comprise a spatially confined solution set (Lumley 1967, 1981). In this regard, Fourier modes differ from POD modes, but in many ways the latter can be treated as synonymous with the former when the field studied is homogeneous, periodic or stationary. In the present analysis, we examine the POD modes of the near pressure field in order to ascertain the degree to which they resemble spatial Fourier modes.

The first 16 POD eigenfunctions, shown in figure 15, illustrate the spatial wave-like characteristics of the POD basis for both nozzles and all flow conditions studied. In the SN flow increased near-nozzle activity occurs. In addition to the energetic pairing observed in the eigenspectra (figure 11), in terms of spatial orgonization the POD basis can here be seen to comprise pairs of modes of similar characteristic wavenumber, similar to a Fourier basis. By looking at the spatial-phase portraits of the eigenfunctions, their resemblence to Fourier modes can be better appreciated. These are shown in figure 16, for eigenfunctions computed from the solution to (4.3). The amplitude of $\phi^{(n)}(x)$ is plotted against that of $\phi^{(m)}(x)$, for $n = 1$ and $m = 1$ to 4 using results obtained from the SCN data at for condition 1. We show only a limited set, as similar behaviour was found for all pairs studied.

The spatial-phase portraits are found to be nearly circular for successive POD mode pairs 1&2, 3&4, ... and indeed this was found to be the case for all successive POD mode pairs $n, m = 2\alpha - 1, 2\alpha$, where $\alpha = 1$ to $N/2$. This constitutes a further means of evaluating how close the POD basis of the pressure field is to a Fourier basis (phase plots of the real and imaginary components of a Fourier basis are perfect circles). The near-circular character of the spatial phase plots, and the near-equal energy of the POD mode pairs, as shown in figure 11, constitute two criteria by which to assess the extent to which these POD modes resemble Fourier modes. This phase pairing was found for both nozzles and all three exit conditions, and is shown in figure 17 using the first two mode pairs $\phi^{(n)}(x)$ and $\phi^{(m)}(x)$, for $\alpha = 1$ to 2.

As a final test of the proximity of the POD basis to a Fourier basis we consider a model system with a highly simplified periodic spatial structure, such that the Fourier transform of a slice through the two-point correlation matrix $R_t(x, x') = \langle p(x, t)p(x', t)\rangle$,

$$\hat{p}(x, \alpha) = \int R_t(x, x')\, \mathrm{e}^{-\mathrm{i}(\alpha x')}\, \mathrm{d}x', \tag{4.8}$$

produces a Fourier basis whose individual energies are related by: $\hat{p}(x, 0) > \hat{p}(x, 1) > \ldots \hat{p}(x, N/2 + 1)$, similar to the eigenvalues in figure 11. For this system,

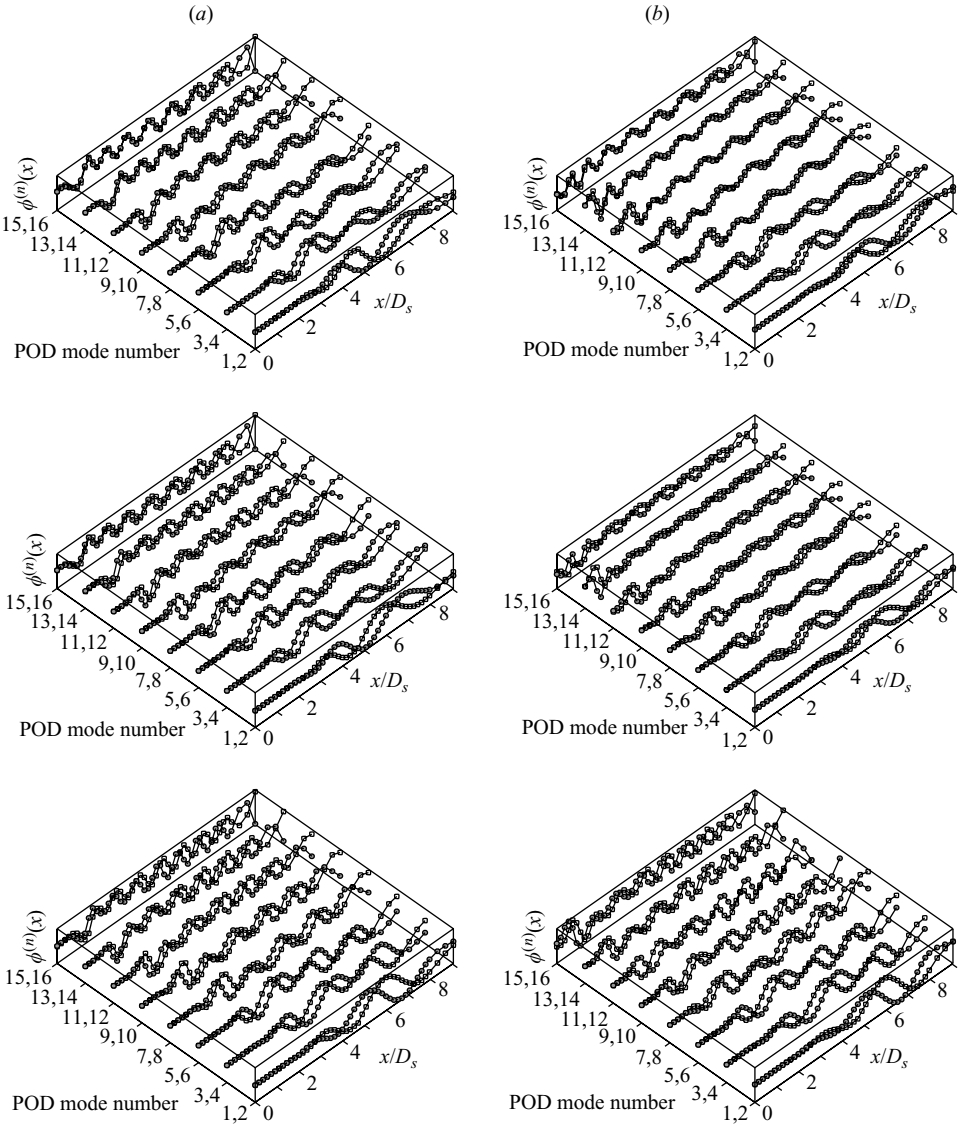

FIGURE 15. First 8 eigenfunction pairs: (*a*) SCN flow; (*b*) SN flow; from top to bottom conditions: 1, 2, 3.

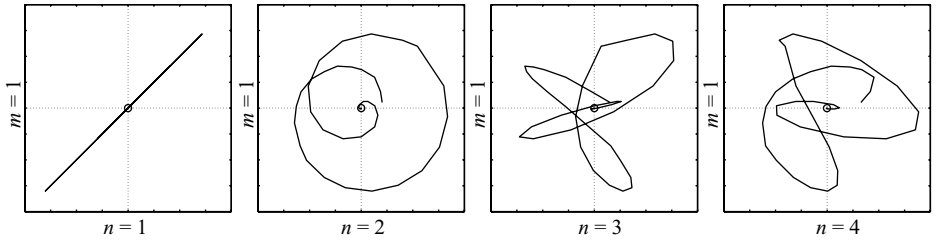

FIGURE 16. Argand diagram of $\phi^{(n)}(x)$ plotted against $\phi^{(m)}(x)$ using the results for condition 1 of the SCN flow.

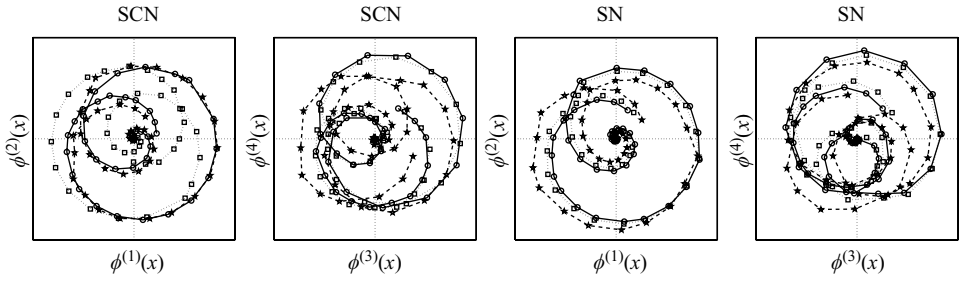

FIGURE 17. Argand diagram of paired modes from the SCN and SN flows under conditions 1 (○), 2 (□) and 3 (⋆).

the complex modulus of the first Fourier coefficient is equal to the energy of the first POD mode, $\hat{p}(x,0)=\lambda^{(1)}$, while the complex moduli of subsequent Fourier coefficients and eigenvalues are related by

$$\hat{p}(x,\alpha) = \lambda^{(2\alpha)}, \quad \hat{p}(x,-\alpha) = \lambda^{(2\alpha+1)}. \tag{4.9a,b}$$

The superscript of the eigenvalues (λ) may switch between (4.9a) and (4.9b) as they relate to the even or odd Fourier coefficients since the odd POD mode does not necessarily lead the even POD mode for a given POD mode pair. A single Fourier wavenumber representation of $R_t(x,x')$, by analogy with a low-order reconstruction of the POD kernel, is given by

$$p^{(\pm\alpha)}(x,x') = \hat{p}(x,\pm\alpha)\,\mathrm{e}^{\mathrm{i}(\pm\alpha x')}. \tag{4.10}$$

And so from (4.5) and (4.10) the Fourier and POD basis sets can be related by

$$\begin{aligned}\hat{p}(x,\alpha)\,\mathrm{e}^{\mathrm{i}(\alpha x')} + \hat{p}(x,-\alpha)\,\mathrm{e}^{\mathrm{i}(-\alpha x')} &= \sum_{n=2\alpha}^{2\alpha+1} \lambda^{(n)}\phi^{(n)}(x)\phi^{(n)}(x') \\ &= \sum_{n=2\alpha}^{2\alpha+1} R_t^{(n)}(x,x'). \end{aligned}\tag{4.11}$$

If the foregoing equations are satisfied then the proper orthogonal and Fourier decompositions are exactly equivalent. In order to assess how close the near pressure fields sampled by the axial array are to this condition, the POD modes are Fourier transformed individually (here we adopt the notation k_x to denote wavenumber, rather than α),

$$A^{(n)}(k_x) = \int \phi^{(n)}(x)\,\mathrm{e}^{-\mathrm{i}(k_x x)}\,\mathrm{d}x. \tag{4.12}$$

As we are not interested in the contribution of the individual eigenfunctions to the overall energy, the eigenvalues $\lambda^{(n)}$ have not been included in the integral of (4.12). The POD–wavenumber spectra which result from this operation are shown in figure 18 for both nozzles and all exit conditions (only positive wavenumbers have been included). For comparative purposes, an equivalent wavenumber k_{eq} is computed and is shown in figure 18. The equivalent wavenumber follows the work of Moser (1994) and is determined as follows:

$$k_{eq}^{(n)2} = \int \left|\frac{\partial\phi^{(n)}}{\partial x}\right|^2 \mathrm{d}x. \tag{4.13}$$

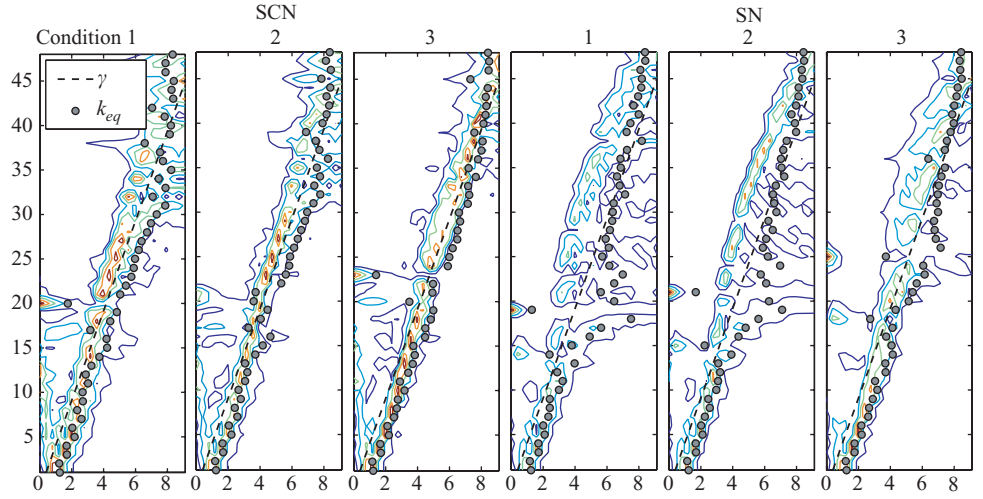

FIGURE 18. Axial wavenumber energy of the POD basis where the abscissa and ordinate axis correspond to the wavelength k [m^{-1}] and POD mode number n, respectively.

The dashed line, denoted by γ, in figure 18 corresponds to a perfect equivalence between the POD and Fourier basis sets (the line is given by (4.9*a*, *b*) with $2n \propto \alpha$). For a given nozzle and jet condition, a contour profile characterizes the Fourier–wavenumber distribution of energy in each POD mode. If the relationships defined by (4.9*a*, *b*), (4.10) and (4.11) were perfectly satisfied, then the contoured profile, the equivalent wavenumber points and the dashed lines would be superposed. While this is not exactly the case, the POD basis set is nonetheless very close to the Fourier basis set, with the energy of each POD mode closely confined to a single, or small finite number of, wavenumbers, even for the higher POD modes.

4.2. *Similarity*

If the pressure field is homogeneous in terms of the characteristic axial wavenumbers, then a self-similar solution should exist from which the scaling of the two-point correlation obtained between two fixed points can be written with a function that only depends on the similarity variables from the self-similar solution. While it has recently been shown by Ewing *et al.* (2007) that an equilibrium solution does exist for the turbulence in the far-field regions of the single-stream jet flow and that the appropriate scaling variable depends only on the separation distance between the similarity coordinate $\ln(x') - \ln(x)$, a similarity solution for the near-jet region ($0 < x/D < 10$) is unavailable (and not possible) since a virtual origin cannot exist. The single-point statistics do however collapse, as shown by many investigators for single-stream jet flows (Bradshaw, Ferriss & Johnson 1964; Hussain & Clark 1981; Kerhervé *et al.* 2004), using the similarity variable $\eta(x) = (r - r_{0.5})/D$ where $r_{0.5}$ is the radial position where the mean velocity is 50 % of the exit velocity. An experiment of Ko & Kwan (1976) showed that by using equivalent variables, the co-axial jet flow demonstrated a self-similar behaviour like that of the single-stream jet. As the large-scale flow events are known to drive the near pressure field of subsonic jet flows (Lau, Fisher & Fuchs 1972; Picard & Delville 2000; Tinney *et al.* 2007), a self-similar behaviour of the near pressure field might be expected. This self-similarity

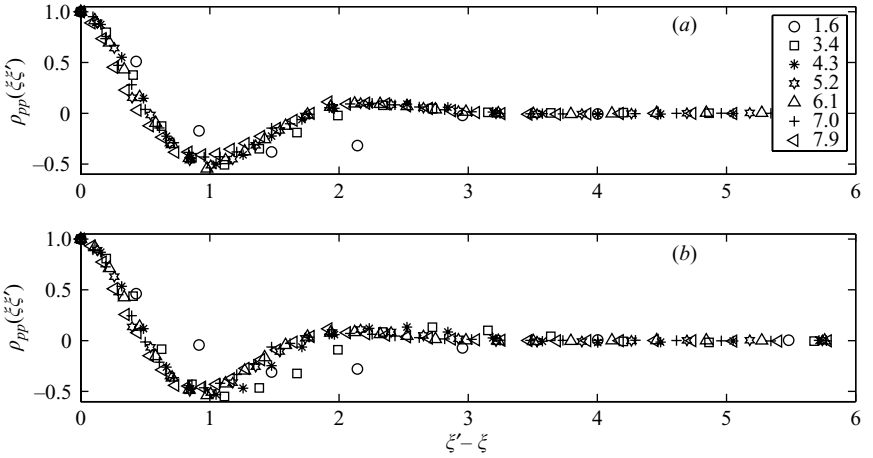

FIGURE 19. The two-point similarity of the pressure along the line array from condition 1 of the (*a*) SCN and (*b*) SN flows.

is demonstrated in figure 19(*a*, *b*) where the normalized two-point cross-correlation,

$$\rho_{pp}(\xi, \xi') = \frac{\langle p(\xi, t)p(\xi', t)\rangle}{\sigma_p(\xi)\sigma_p(\xi')}, \tag{4.14}$$

is plotted as a function of the same similarity variables as Ewing *et al.* (2007), that is, $\xi' - \xi = \ln(x') - \ln(x)$. Here $\sigma_p(\xi)$ is the standard root-mean-square pressure at position ξ. The failure of the profiles to collapse near the nozzle exit is consistent with the findings of Bradshaw *et al.* (1964), Ko & Davies (1971) and Arndt Long & Glauser (1997).

5. Acoustic–hydrodynamic filtering

This section is devoted to addressing two problematic issues, already mentioned in the introduction, which need to be considered when analysing pressure measurements in the irrotational near field of a turbulent jet. The first is the problem of ascertaining to what degree the measured pressure fluctuations comprise hydrodynamic and/or acoustic contributions. The second is the difficulty of relating such pressure measurements to an underlying source mechanism.

5.1. *k_x–f spectra: acoustic and hydrodynamic signatures*

It has been found by Arndt *et al.* (1997) and Coiffet *et al.* (2006), that in the near irrotational pressure field of a jet a meaningful distinction can be drawn between pressure fluctuations which carry the convective footprint of the underlying turbulence, for example low-pressure signatures associated with the passage of vortex cores (Lau *et al.* 1972; Picard & Delville 2000; Tinney *et al.* 2007), which we designate as hydrodynamic, this component being synonymous with pseudosound (Ribner 1964), and acoustic pressure fluctuations which are characterized by spherical, sonic propagation. In Guitton *et al.* (2007) the near pressure field of a jet is shown to comprise a superposition of these distinctly different kinds of fluctuation.

A criterion is therefore available for the removal of all acoustic pressure fluctuations from the near-field measurements. As depicted in figure 20, for a sound field generated by sources on the same axis as the array (source distribution A), the phase velocity

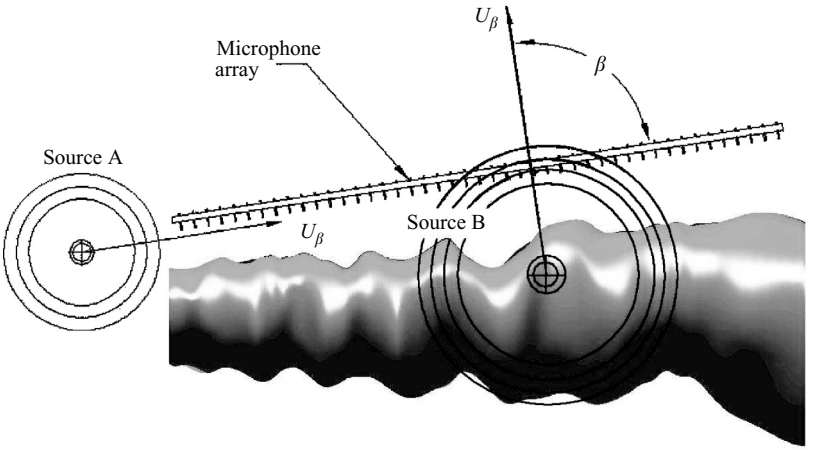

FIGURE 20. Schematic of the source field relative to the microphone array.

registered on the array is equal to the speed of sound. For a sound field generated by sources at some distance normal to the array axis (source B) the phase velocity is much higher: in the far field limit, where the sound waves arriving at the array are plane, the phase velocity registered in this case is infinite. Assuming that the array is located in a region of zero mean velocity, *no sound field can produce a subsonic phase velocity on the array*.

In order to isolate components of the pressure field characterized by either subsonic or supersonic phase velocity, a two-dimensional Fourier transform of the pressure field is performed $p(x, t) \longrightarrow p(k_x{-}f)$ according to

$$p(k_x{-}f) = \frac{1}{2\pi} \int \int p(x, t) W(x) \mathrm{e}^{-\mathrm{i}(k_x x + 2\pi f t)} \, \mathrm{d}x \, \mathrm{d}t. \tag{5.1}$$

A window function $W(x)$ is included in the spatial transform in order to ensure that the boundaries are smooth, and a cubic spline interpolation is performed in order to improve the axial resolution of the sypatial grid (figure 21). The resulting ensemble-averaged wavenumber–frequency spectra are given by

$$\hat{P}(k_x{-}f) = \langle p(k_x{-}f) p^*(k_x{-}f) \rangle, \tag{5.2}$$

where * denotes a complex conjugate. Spectra (hereafter $k_x{-}f$ spectra) were computed for both nozzles and all three exit conditions, and these are shown in figure 22(a, b). Frequency and axial wavenumber, which are shown, respectively, on the horizontal and vertical axes, have been non-dimensionalized using the diameter and velocity of the secondary nozzle/flow.

The two spectral lobes in the $k_x{-}f$ spectra, whose levels and extent vary as a function of the exit condition, are associated with a rich variety of physical phenomena which we will discuss here. The near pressure field is essentially driven by the turbulent fluctuations of the flow. But the turbulence is extended in the radial direction and comprises two major mixing regions in the form of two annular shear layers. The shear layer between the primary and secondary flows is characterized by mean convection velocities lying somewhere between the two jet velocities, while the external shear layer, between the secondary flow and the ambient air, is characterized by mean convection velocities somewhat lower than that of the secondary flow. In addition, these mixing layers excite sound waves which are characterized by spherical propagation. These

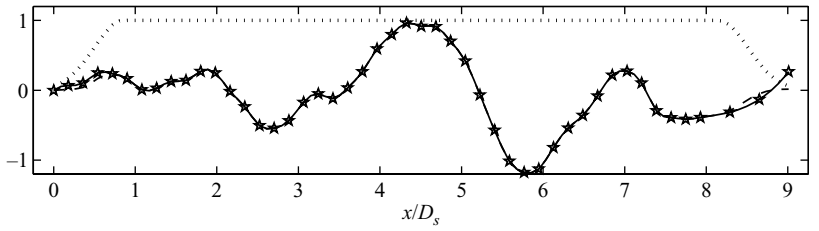

FIGURE 21. The window function (···) along with a pressure time series snapshot from the original grid (⋆), its cubic interpolation (−), and the effects of the window function on the cubic interpolation (−−).

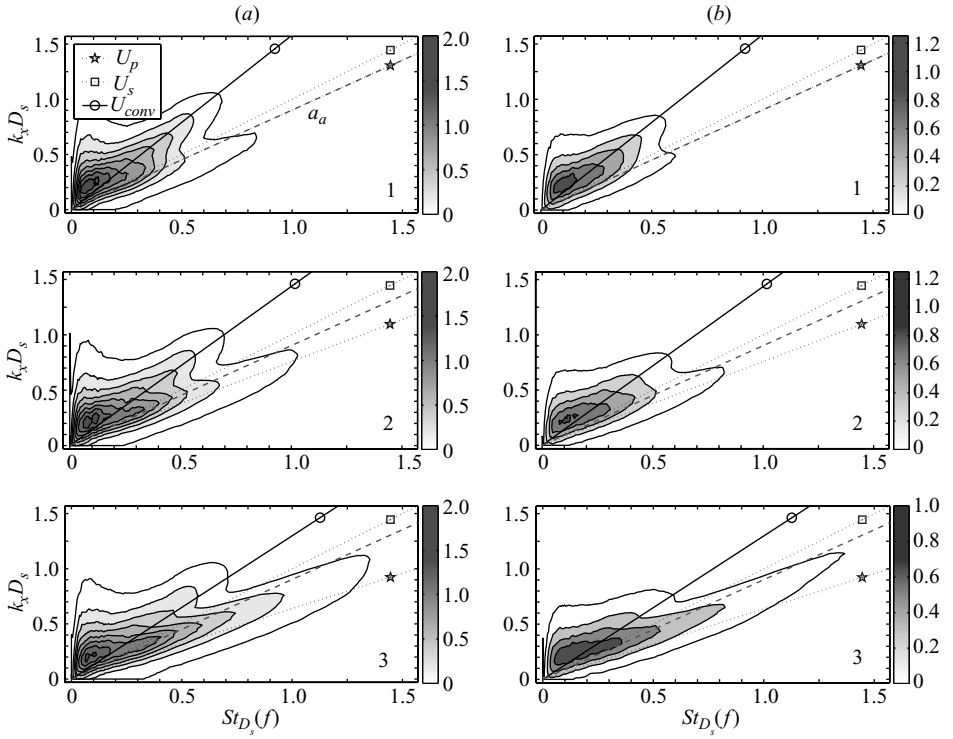

FIGURE 22. Ensemble-averaged wavenumber–frequency spectra $\hat{P}(k_x{-}f) \times 10^{-6}$ for the (*a*) SCN and (*b*) SN flows under different jet exit conditions 1, 2, 3 (top to bottom). A thick solid line identifies the convection velocity using equation (5.3), while dotted lines identify the exit speeds of the primary and secondary flows. The sound speed of the ambient air (a_a) is identified by the dashed line. The slope of the supersonic signature (below the dashed line) indicates the dominant acoustic radiation angles. These are approximated for SCN (condition 1,2,3) = 35°, 36°, 34° and for SN (condition 1,2,3) = 38°, 34°, 34°.

different phenomena will each produce a signature in the $k_x{-}f$ spectra, depending on their respective energies, their characteristic convection or propagation velocities, and the radial extent of their zone of influence (hydrodynamic signatures, for example, decay much more quickly than acoustic signatures).

In view of these various characteristics, a number of lines have been added to figure 22(*a*, *b*), whose slopes correspond to different phase velocities along the array.

The first corresponds to a global convection velocity defined by

$$U_{conv} = 0.60\left(\frac{U_s + U_p}{2}\right). \tag{5.3}$$

The lines $f = k_x U_p$ and $f = k_x U_s$ (denoted U_s and U_p in the legend of figure 22*a*) correspond to primary and secondary flow velocities respectively (as given in table 1), and the dashed line, denoted a_a in the top left figure, corresponds to $f = k_x a_a$. The latter provides a means of separating hydrodynamic and acoustic pressure fluctuations: spectral components above a_a are characterized by subsonic phase velocities, and can be associated with purely hydrodynamic fluctuations, while components on and below a_a correspond to propagating (acoustic) pressure fluctuations. The lines U_s and U_p help ascertain, for a given exit condition, whether either of the mixing layers could have produced a given spectral distribution by means of a convection-dominated phenomenon.

The strongest signature observed in the spectra comprises a subsonic lobe with a peak at $(k_x D_s, St_{D_s}) = (0.2, 0.1)$, and a portion aligned with U_{conv}. This indicates that the predominant contribution to the near-field pressure fluctuations comes from flow structures characterized by a convection velocity somewhat lower than that of the secondary flow, and which are thus to be found in the outer mixing layer.

The amount of spread about the line $f = k_x U_{conv}$ provides a measure of how dispersive the hydrodynamic component of the pressure field is. Because of this spread certain hydrodynamic components of the pressure signature generated by the convected structures will be found on the supersonic side of the sonic line a_a. Such components are acoustically matched, and thus synonymous with the birth of a sound field.

The second spectral lobe falls primarily in the acoustic region of $(k_x{-}f)$ (i.e. beneath the sonic line a_a). The lines U_s and U_p can help shed light on the nature of the physical mechanisms which give rise to this supersonic signature. They show how the slope of the supersonic spectral lobe exceeds both flow velocities for condition 1. This is an indication that the supersonic signature must be attributed, for this exit condition, to a combination of: (i) supersonic components related to the growth and decay of the mixing-layer structures (see Crighton & Huerre (1990) for further discussion regarding this phenomenon and its importance for sound production); and (ii) to further propagative fluctuations which were generated at some distance normal to the array, and which have therefore left their hydrodynamic cause well behind them within the rotational region of the flow. The latter fluctuations will be characterized by higher phase velocities. The supersonic lobe becomes considerably enhanced for conditions 2 and 3 due to the increased exit velocities of the primary jet. In these cases the inner mixing layer can produce this signature by purely convective phenomena, and so there is here a possibility of Mach-wave type sound production, *if these mixing-layer structures are efficient in driving pressure fluctuations in the irrotational near field where the ambient sound speed is lower than their convection velocity*. This is probably only true in the downstream regions of the flow, where the mixing layers merge.

5.2. *Acoustic–hydrodynamic filtering*

Aside from a global reduction in energy, the structural changes produced by the serrations are too slight to be visible in the $k_x{-}f$ spectra. However, by filtering the $k_x{-}f$ spectra such that only energy in either the subsonic or the supersonic regime is

retained, a double inverse Fourier transform,

$$p_{sub}(x,t) = \int\int p(k_x > f/a_a,\, f < k_x a_a) \mathrm{e}^{j(k_x x + 2\pi f t)}\, \mathrm{d}k_x\, \mathrm{d}f, \tag{5.4}$$

$$p_{super}(x,t) = \int\int p(k_x < f/a_a,\, f > k_x a_a) \mathrm{e}^{j(k_x x + 2\pi f t)}\, \mathrm{d}k_x\, \mathrm{d}f, \tag{5.5}$$

allows the space–time structure of the hydrodynamic (5.4) and acoustic (5.5) components of the pressure fields to be recovered and analysed. This allows some of the more subtle changes to be identified.

The result of this operation is shown in figure 23(a, b) for an arbitrarily selected sample of data (no ensemble averaging has been applied), acquired at jet condition 1 using both the SCN (figure 23a) and SN (figure 23b) flows. For each of the data sets, the space time structure of the original time series is compared with its hydrodynamic (5.4) and acoustic (5.5) components. The dashed lines plotted on the hydrodynamic and acoustic fields identify, respectively, the convection and propagation velocities, U_{conv} and a_a.

5.3. *Hydrodynamic components*

The hydrodynamic field (filtered using $f < k_x a_a$) is globally very similiar to the unfiltered field (figure 23a, b), showing again how the pressure field is predominantly comprised of hydrodynamic fluctuations. The subsonic structure is seen to be globally smoother than the unfiltered field, due largely to the removal of less coherent 'ripples' associated with the high-frequency sound field. This was observed for all flow conditions, with and without serrations. Also, the effects of the primary jet on the hydrodynamic signature can be seen in the downstream regions of the measurement domain where the characteristic convection velocity can be seen to increase with increasing x.

5.4. *Acoustic components*

The field filtered using $f > k_x a_a$ (supersonic components retained) shows two interesting features. The first is the dominance of axially coherent structures†, whose phase velocity is close to the speed of sound. This indicates a coherent sound field which propagates at small angles to the array axis. The second interesting feature is a less organized signature, characterized by higher-frequency, more spatially localized events (i.e. weaker axial coherence) and substantially higher phase velocity. This signature is characteristic of a high-frequency sound field radiating normal to the line array.

Now with respect to some current ideas regarding the dominant source mechanisms in subsonic jets these signatures are of some interest. A jet is thought to produce sound by two different mechanisms. The first is thought to be related to coherent flow structures, first identified as important in the 1970s and 1980s (Bradshaw *et al.* 1964; Ko & Davies 1971; Hussain & Clark 1981) and which are believed to dominate radiational shallow angles to the jet. While there is no real consensus as to the precise mechanisms which underlie this source component, some popular candidates for the single-stream jet include vortex pairing (Laufer & Yen 1983), wavy-wall-type mechanisms (Ffowcs Williams & Kempton 1978; Crighton & Huerre 1990; Coiffet *et al.* 2006), and vortex eigenoscillations (Kopiev *et al.* 1999), all of which are believed

† In figure 23 the colour scales between the subsonic and supersonic components are not comparable due to the large-amplitude disparities between them.

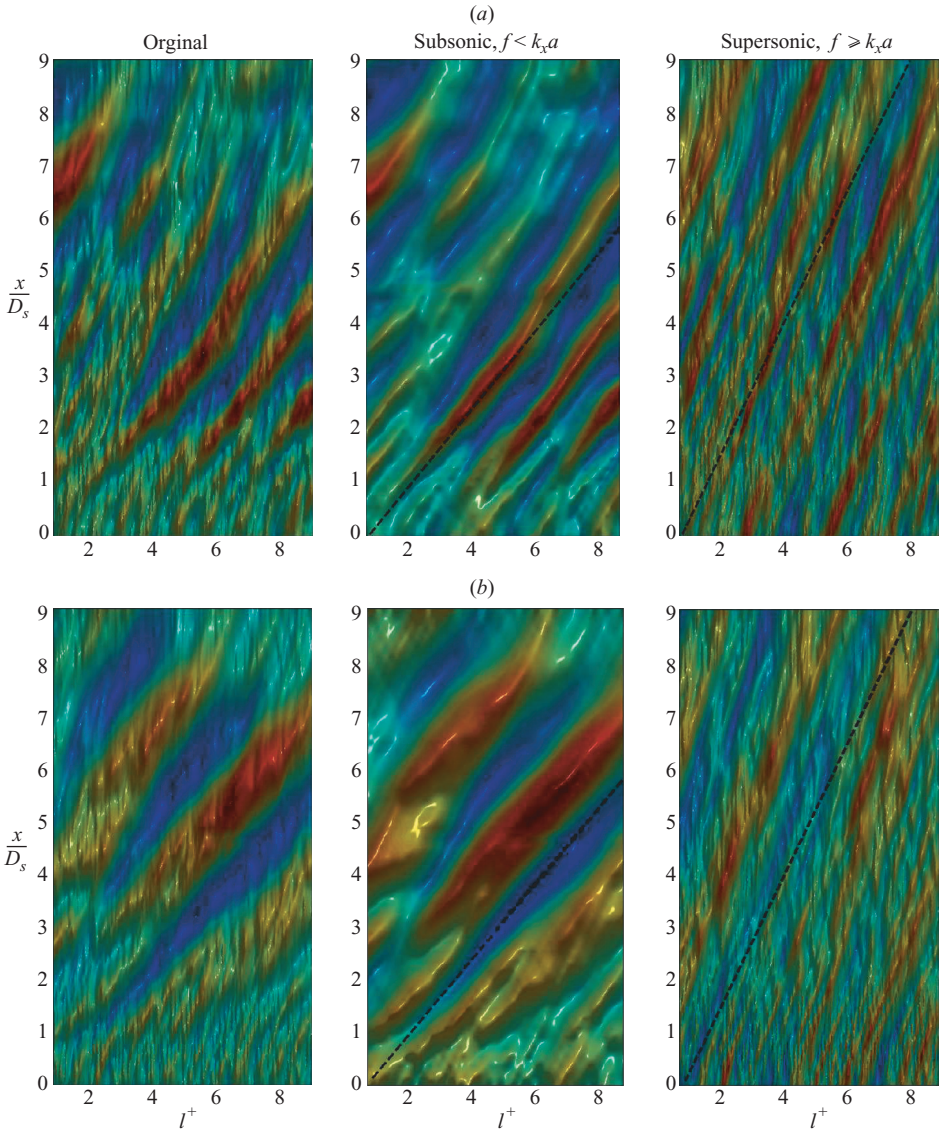

FIGURE 23. Reconstruction of the original and wavenumber-filtered pressure data (space–time) under condition 1 for the (*a*) SCN and (*b*) SN flows. The units on the *x*-axis are $t^+ = tU_s/D_s$ and lines corresponding to U_{conv} and a_a are shown on the subsonic and supersonically filtered fields.

to dominate in the initial mixing-layer region of the flow, and high-energy intermittent events associated with the collapse of the potential core (Juvé, Sunyach & Comte-Bellot 1980; Bogey, Bailly & Juvé 2003; Viswanathan *et al.* 2006; Citriniti & George 2000). The second source component is thought to be related to the fine-scale random turbulence (Tam, Golebiowski, & Seiner 1996); this component is believed to radiate more omnidirectionally, and to dominate the far-field spectra at large angles to the jet (see the review paper by Jordan & Gervais (2008) and the work of Laurendeau *et al.* (2008) for further discussion of the mechanisms which may underlie these signatures). The axially coherent signature evident in the supersonically filtered pressure field in

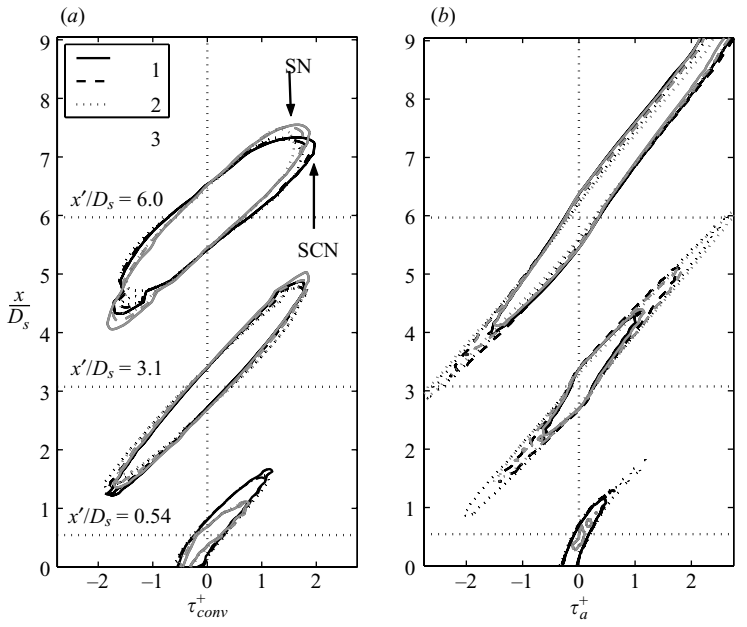

FIGURE 24. Normalized space–time correlations of (*a*) the subsonic and (*b*) the supersonically filtered pressure fields. Non-dimensional time-delay coordinates have been used: subsonic correlation $\tau^+_{conv} = tU_{conv}/D_s$; supersonic $\tau^+_a = ta_a/D_s$. Only the 0.4 contour is shown.

figure 23(a, b) supports the idea of an organized source mechanism which radiates at small angles to the jet, and whose sound waves remain coherent over a distance of the order of about $5D_s$. This component appears to have been generated somewhere between $x/D_s = 3$ and $x/D_s = 5$ in the SCN flow.

The effects of the serrations are also clearly visible: the high-energy low-frequency coherent component of the sound field has been attenuated, while the less-coherent high-frequency component has been enhanced, particularly in the near-nozzle region.

Space–time correlations were generated from the subsonic and supersonically filtered fields, and are shown in figure 24, for all three jet exit conditions and for the SN and SCN flows. The contour level 0.4 is shown for correlations computed at three different locations: $x' = 0.54$, 3.1 and 6. As with the frequency–wavenumber spectra, structural differences are slight. The convection velocity of the hydrodynamic component has been slightly increased in the downstream region ($x/D_s = 6$); the axial coherence in the near-nozzle region has been slightly reduced. In figure 24(b) we see that the axial coherence of the acoustic component has been reduced in the initial mixing-layer region ($x/D_S = 0.5$; $x/D_S = 3$), whereas at $x/D_S = 6$ there is almost no structural difference between the sound fields. This demonstrates that the sound source mechanisms, thought less efficient in the serrated-nozzle flow, have not been subjected to any fundamental structural changes in the downstream regions of the jets, where source activity is most intense.

A more quantitative illustration of the relative contributions from the acoustic and hydrodynamic components to the overall near pressure field is provided by figure 25. The mean-square pressure of the subsonic and supersonically filtered fields has been integrated over the axial measurement range for each of the conditions studied (The total mean-square pressure is equal to the sum of contributions from

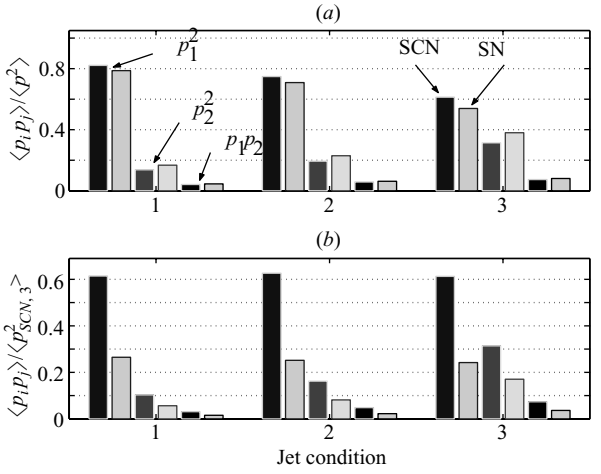

FIGURE 25. Hydrodynamic (the two left-hand columns of each set, p_1), acoustic (the middle two columns, p_2) and cross-term (the right-hand two columns, $p_1 p_2$) energies, integrated over axial position and frequency: (*a*) normalized by total integrated energy of jet condition considered; (*b*) normalized by total integrated energy of SCN, condition 3. The left-hand column of each pair is for SCN, and the right-hand use for SN.

the subsonic component (p_1^2), the supersonic component (p_2^2) and their product ($p_1 p_2$).) In figure 25(*a*) each integrated value has been normalized by the total mean-square value of the corresponding flow condition: this provides a means of comparing the hydrodynamic/acoustic composition between different flows. As the bypass ratio decreases the relative contribution from the acoustic component increases, not surprisingly, as decreases in the bypass ratio have been seen to lead to greater far field levels. However, more interestingly, we see that the serrations lead to a higher relative contribution from the acoustic component. Figure 25(*b*), where all values have been normalized by the total energy of SCN condition 3, allows comparisons in terms of the absolute values: we see that the hydrodynamic component changes very little with changes in the bypass ratio, while serrations lead to reductions of the order of 50%, for both the hydrodynamic and the acoustic components. It is important to remember however, that the interpretational difficulties mentioned in the introduction of this paper (due primarily to uncertainties regarding the amount of information which has been lost with respect to the structure of the pressure field within the mixing region of the flow) prevent the drawing of more definite conclusions regarding the relationship between the hydrodynamic and acoustic fluctuations.

6. Conclusion

Data from measurements performed in the near pressure fields of a number of co-axial jets (with and without serrations, and where bypass ratio and temperature ratio are varied) have been presented.

The study shows that serrations produce considerable reductions in the near-field pressure *levels*; however *structural changes* in the flows are more subtle. The low-frequency, predominantly hydrodynamic portion of the pressure spectrum was found to be most influenced by the turbulence of the outer mixing layer, changes in the primary-jet exit conditions having negligible effect. The higher frequency,

predominantly acoustic portions of the pressure spectra on the other hand were found to be strongly influenced by changes in the primary-jet exit conditions at locations downstream of $x/D_s = 4$. This was found to be the case both for the serrated and un-serrated nozzles, and is attributed to the additional mixing region which is produced by changes in the bypass ratio (as a result of the interaction of the inner and the outer shear layers).

A POD analysis was performed using both a time-averaged kernel, and a kernel comprising cross-spectral densities. Both solutions illustrated the growth, saturation and decay process of axial instabilities. The solution to the time-averaged kernel was shown to produce a basis-function set which resembles a Fourier basis-function set in many ways. The pressure line-array data was also found to collapse quite well using the similarity variables of Ewing *et al.* (2007).

A two-dimensional Fourier transform from $p(x, t)$ to $p(k_x–f)$ was used to study the pressure fields in wavenumber–frequency space. A filtering operation, based on the dispersion inequality $f > ka$, was used to reconstruct of the hydrodynamic and acoustic components of the near pressure field and the space–time characters of these fields were compared. Two distinct acoustic features were observed, related, respectively, to components radiating at small and large angles to the jet axis. The former component was found to be dominated by axially coherent low-frequency signatures, while the latter was found to be dominated by less-organized, higher-frequency fluctuations. These observations are consistent with the two similarity spectra proposed by Tam *et al.* (1996); however, the dynamics of the jet responsible for each of these signatures remain poorly understood. These near-field measurements, filtered as we have done here, provide a valuable experimental opportunity to further probe this question, and this is the object of further work.

This work was funded by the EU program CoJeN (AST3-CT-2003-502790). The authors would also like to acknowledge the support of the staff of the NTF (Noise Test Facility), QinetiQ, whose participation in the experimental campaign was invaluable, also DLR (Ulf Michel and Sébastien Guérin) both for supplying the microphones and for their participation in the experiment, ISVR (Juan Battaner-Moro) for provision of an acquisition system and for assistance provided in setting up the experiment, the University of Warwick (Andrew Skeen and Paul Dunkley) for the provision of the PIV data, and to Louis Huet, Patrick Laurent, Jean-Marc Mougenot and the workshop staff of the Centre d'Etudes Aérodynamique et Thermique (CEAT), Poitiers, for their part in the design of the near field arrays. Finally, the authors are grateful to Kevin Britchford (Rolls Royce) and Craig Mead (QinetiQ) for coordinating the experimental campaign and to Joël Delville for many helpful discussions.

REFERENCES

Alkislar, M. B., Krothapalli, A. & Butler, G. W. 2007 The effect of streamwise vortices on the aeroacoustics of a Mach 0.9 jet. *J. Fluid Mech.* **578**, 139–169.

Arndt, R. E. A., Long, D. F. & Glauser, M. N. 1997 The proper orthogonal decomposition of pressure fluctuations surrounding a turbulent jet. *J. Fluid Mech.* **340**, 1–33.

Aubry, N., Holmes, P., Lumley, J. & Stone, E. 1988 The dynamics of coherent structure in the wall region of a turbulent boundary layer. *J. Fluid Mech.* **192**, 115–173.

Barré, S., Bogey, C., Fleury, V., Bailly, C. & Juvé, D. 2006 Experimental study of the properties of near field and far field jet noise. *AIAA Paper* 2006-2649.

Berkooz, G., Holmes, P. & Lumley, J. L. 1993 The Proper Orthogonal Decomposition in the analysis of turbulent flows. *Annu. Rev. Fluid Mech.* **25**, 539–575.

Bogey, C., Bailly, C. & Juvé, D. 2003 Noise investigation of a high subsonic, moderate Reynolds number jet using compressible large eddy simulation. *Theor. Comput. Fluid Dyn.* **16**, 273–297.

Bradshaw, P., Ferriss, D. H. & Johnson, R. F. 1964 Turbulence in the noise-producing region of a circular jet. *J. Fluid Mech.* **19**, 591–624.

Brown, C. A. & Bridges, J. 2006 Acoustic efficiency of azimuthal modes in jet noise using chevron nozzles. *AIAA Paper* 2006-2654.

Citriniti, J. H. & George, W. K. 2000 Reconstruction of the global velocity field in the axisymmetric mixing layer utilizing the proper orthogonal decomposition. *J. Fluid Mech.* **418**, 137–166.

Coiffet, F., Jordan, P., Delville, J., Gervais, Y. & Ricaud, F. 2006 Coherent structures in subsonic jets: a *quasi*-irrotational source mechanism? *Intl J. Aeroacoust.* **5**, 67–89.

Crighton, D. G. & Huerre, P. 1990 Shear layer pressure fluctuations and superdirective acoustic sources. *J. Fluid Mech.* **220**, 355–368.

Delville, J., Ukeiley, L., Cordier, L., Bonnet, J. P. & Glauser, M. N. 1999 Examination of large scale structures in a turbulent plane mixing layer. Part 1. Proper Orthogonal Decomposition. *J. Fluid Mech.* **391**, 91–122.

Ewing, D., Frohnapfel, B., George, W. K., Pedersen, J. M. & Westerweel, J. 2007 Two-point similarity in the round jet. *J. Fluid Mech.* **577** 309–330.

Ffowcs Williams, J. E. & Kempton, A. J. 1978 The noise from the large-scale structure of a jet. *J. Fluid Mech.* **84**, 673–694.

Freund, J. B. 2001 Noise sources in a low-Reynolds-number turbulent jet at Mach 0.9. *J. Fluid Mech.* **438**, 277–305.

George. W. K., Beuther, P. D. & Arndt, R. E. A. 1984 Pressure spectra in turbulent free shear flows. *J. Fluid Mech.* **148**, 155–191.

Glauser, M. N. & George, W. K. 1987 Orthogonal decomposition of the axisymmetric jet mixing layer including azimuthal dependence. *Advances in Turbulence* (ed. G. Comte-Bellot & J. Mathieu), pp. 357–366. Springer.

Guerin, S. & Michel, U. 2006 Circumferential analysis of the near pressure field of a co-axial subsonic jet. Presented at 10th CEAS-ASC Workshop: Jet Noise Prediction Methodologies, Recent Developments. Dublin, Ireland.

Guitton, A., Jordan, P., Laurendeau, E. & Delville, J. 2007 Velocity dependence of the near pressure field of subsonic jets: understanding the associated source mechanisms. *AIAA Paper* 2007-3661.

Harper-Bourne, M. 2004 On modelling the hydrodynamic field of high-speed jets *10th AIAA/CEAS Aeroacoustics conference, Manchester, May 2004.*

Howes, W. L. 1960 Distribution of time-averaged pressure fluctuations along the boundary of a round subsonic jet. *NASA Tech. Note* D-468.

Hussain, A. K. M. F. & Clark, A. R. 1981 On the coherent structure of the axisymmetric mixing layer: a flow-visualization study. *J. Fluid Mech.* **104**, 263–294.

Jordan, P. & Gervais, Y. 2008 Subsonic jet aeroacoustics: associating experiment, modelling and simulation. *Exps. Fluids* **44**, 1–21.

Jordan, P., Tinney, E., Delville, J., Coiffet, F., Glauser, M. N. & Hall, A. 2005 Low-dimensional signatures of the sound production mechanisms in subsonic jets: Towards their identification and control. *AIAA Paper* 2005-4647.

Juvé, D., Sunyach, M. & Comte-Bellot, G. 1980 Intermittency of the noise emission in subsonic cold jets. *J. Sound Vib.* **71**, 319–332.

Keast, D. N. & Maidanik, G. Studies in the near field of noise properties of a small air jet. *Bolt, Beranek and Newman, Report 1272, February 1966.*

Kerhervé, F., Jordan, P., Gervais, Y., Valière, J. C. & Braud, P. 2004 Two-point laser doppler velocimetry measurements in a Mach 1.2 cold supersonic jet for statistical aeroacoustic source model. *Exps. Fluids* **37**, 419–437.

Ko, N. W. M. & Davies, P. O. A. L. 1971 The near field within the potential cone of subsonic cold jet. *J. Fluid Mech.* **50**, 49–78.

Ko, N. W. M. & Kwan, S. H. 1976 The initial region of subsonic coaxial jets. *J. Fluid Mech.* **73**, 305–332.

Kopiev, V. F., Zaitsev, M. Yu., Chernyshev, S. A. & Kotova, A. N. 1999 The role of large-scale vortex in a turbulent jet noise. *AIAA Paper* 1999-1839.

Lau, J. C., Fisher, M. J. & Fuchs, H. V. 1972 The intrinsic structure of turbulent jets. *J. Sound Vib.* **22**, 379–406.

Laufer, J. & Yen, T. 1983 Noise generation by a low Mach number jet. *J. Fluid Mech.* **134**, 1–34.

Laurendeau, E., Jordan, P., Delville, J. & Bonnet, J.-P. 2008 Source mechanism identification by near field-far field pressure correlations in subsonic jets. *Intl J. Aeroacous.* **7**, 41–68.

Lumley, J. L. 1967 The structure of inhomogenous turbulent flows. In *Atmospheric Turbulence and Radio Wave Propagation* (ed A. M. Yaglom & V. I. Tatarski), pp. 166–178. Moscow: Nauka.

Lumley, J. L. 1981 Coherent structure in turbulence. In *Transition and Turbulence* (ed. R. E. Meyer), p. 215. Academic.

Mayes, W. H., Lanford, W. E. & Hubbard, H. H. 1959 Near-field and far-field noise surveys of solid-fuel rocket engines for a range of nozzle exit pressures. *NASA Tech. Note* D-21.

Mollo-Christensen, E. 1963 Measurements of near field pressure of subsonic jets. *NATO AGARD Rep.* 449.

Moser, R. D. 1994 Kolmogorov inertial range spectra for inhomogeneous turbulence. *Phys. Fluids* **6**, 794–801.

Ollerhead, J. B. 1967 On the prediction of the near field noise of supersonic jets. *NASA Rep.* CR-857.

Picard, C. & Delville, J. 2000 Pressure velocity coupling in a subsonic round jet. *Intl J. Heat Fluid Flow* **21**, 359–364.

Reba, R., Narayanan, S., Colonius, T. & Suzuki, T. 2005 Modeling jet noise from organized structures using near-field hydrodynamic pressure. *AIAA Paper* 2005-3093.

Ribner, H. S. 1964 The generation of sound by turbulent jets. *Adv. Appl. Mech.* **8**.

Ricaud, F. 2003 Étude de l'identification des sources acoustiques è partir du couplage de la pression en champ proche et de l'orgonization instantanée de la zone de mélange de jet. *PhD Thesis*, l'Université de Poitiers, Potiers, France.

Skeen, A. 2007 The development of high-speed PIV techniques and their application to jet noise measurements. PhD Dissertation, University of Warwick, UK.

Suzuki, T. & Colonius, T. 2006 Instability waves in a subsonic round jet detected using a near-field phased microphone array *J. Fluid Mech.* **565**, 197–226.

Tam, C., Golebiowski, M. & Seiner, J. 1996 On the two components of turbulent mixing noise from supersonic jets. *AIAA Paper* 1996-1716.

Tester, B. J. & Fisher, M. J. 2006 A contribution to the understanding and prediction of jet noise generation by forced mixers: Part III applications. *AIAA Paper* 2006-2542.

Tinney, C. E., Jordan, P., Hall, A., Delville, J. & Glauser, M. N. 2007 A Time-resolved estimate of the turbulence and sound source mechanisms in a subsonic jet flow. *J. Turbul.* **8**(7), 1–20.

Viswanathan, K., Shur, M. L., Spalart, P. R. & Strelets, M. K. 2006 Computation of the flow and noise of round and beveled nozzles. *AIAA Paper* 2006-2445.

Wills, J. A. B. 1964 On convection velocities in turbulent shear flows. *J. Fluid Mech.* **20**, 417–432.